Organic carbon burial drivers in the northeastern South China ~~s~~Sea since the last glacial

Any scientific changes (including authorship and funding information) introduced at this stage are subject to review and written approval by editor and/or research integrity specialist prior to consideration and may delay the publication.

Xiao Huang[a], Xinqing Zou[a,b], Zhuoyue Zhang[a], Yadi Zhou[a,b], Chuchu Zhang[a,b], Xuejiao Jiang[a,b,c], Chendong Ge[a,*], gcd@nju.edu.cn, Ruxi Dou[a,b,c], Yue Xue[a], Chenglong Wang[a,**], clwang@nju.edu.cn

[a]School of Geography and Ocean Science, Ministry of Education Key Laboratory for Coast and Island Development, Nanjing University, Nanjing, 210023, China

[b]Collaborative Innovation Center of South China Sea Studies, Nanjing University, Nanjing, 210093, China

[c]Key Laboratory of Marine Geology and Metallogeny, First Institute of Oceanography, Ministry of Natural Resources, Qingdao, 266061, China

*Corresponding author.

**Corresponding author.

Abstract

Marginal seas are important repositories of both terrestrial and marine organic carbon (OC), accounting for over 90% of the global marine sedimentary OC burial flux. The northeastern South China Sea (NESCS), as the largest semi-enclosed marginal sea in the western Pacific, provides an exceptional natural laboratory to investigate millennial-scale OC dynamics. This study analyzes total organic carbon (TOC), stable carbon isotopes ($\delta^{13}C$), radiocarbon isotopes (^{14}C), and lignin phenols in Core S04 from the Taiwan Shoal to examine OC burial variations and their environmental controls since ~36.5 ka.

The results show that deep-water OC burial in the NESCS is not simply controlled by variations in organic matter inputs. Instead, it reflects the combined influence of sea-level-controlled source–sink configuration, monsoon-driven sedimentary dynamics, and pre-depositional reworking and mineral protection processes. During MIS 3, relatively high TOC contents indicate OC burial under a stable source–sink configuration, dominated by marine-derived inputs with a secondary contribution from terrestrial biospheric carbon. During MIS 2, extremely low sea level produced two contrasting regimes. The early to middle glacial period was characterized by high-energy cross-shelf transport and intense particle sorting, which suppressed OC loading efficiency. In contrast, the subsequent deglacial period saw enhanced retention of fine particles and intensified sediment reworking, leading to longer OC residence times and older apparent radiocarbon ages. During the Holocene, strengthened East Asian Summer Monsoon conditions increased terrestrial material supply, but high sea level combined with persistent bottom-current activity maintained a low-loading stable state, in which OC preservation became weakly responsive to source variations and increasingly controlled by transport and reworking processes. Overall, OC burial in the deep basin of the NESCS reflects the coupled effects of climatic forcing and sedimentary transport–preservation processes. These findings provide new process-based constraints on the response of deep-water carbon sinks in continental margin systems to glacial–interglacial climate variability.

Keywords:

Organic carbon; Marginal seas; Source–sink processes; Glacial–interglacial cycles; OC loading

Data availability

All data and/or code is contained within the submission.

1 Introduction

Glacial–interglacial cycles represent the central feature of Quaternary climate variability, accompanied by regular fluctuations of approximately 100 ppmv in atmospheric CO_2 concentration (Lüthi et al., 2008; Kohfeld and Ridgwell, 2009; Brovkin et al., 2012; Bereiter et al., 2015). Numerous studies indicate that the transport and burial of OC within the land-ocean system play a critical role in regulating millennial-scale carbon cycle variations and their coupling with climate (Cartapanis et al., 2016; Shi et al., 2024; Zhao et al., 2024; Wang and Wang, 2025). Unlike the modern carbon cycle, where anthropogenic influences dominate, geological records of OC burial preserve the response and feedback of natural carbon reservoirs to climatic forcing, providing key constraints on long-term climate-carbon interactions. However, the mechanisms controlling OC burial across glacial–interglacial transitions and their variation among depositional settings remain unclear. (Cartapanis et al., 2018; LaRowe et al., 2020).

Although marginal seas occupy only ~10% of the global ocean sarea, they account for about 90% of global marine OC burial flux (Burdige, 2007; Hu et al., 2014; Cui et al., 2016b). Among them,deep-water marginal basins (>2000 m water depth) occupy the terminal position of the shelf-slope-basin system and represent major long-term sinks for terrigenous OC (OC_{terr}). Being remote from high-energy hydrodynamic processes, OC burial in such environments is often not a direct response to climatic boundary conditions alone, but instead records substantial modification by cross-shelf transport, resuspension-redeposition, and early diagenetic processes (Kao et al., 2006a; Cartapanis et al., 2016; Zhang et al., 2023).

OC burial in deep-sea sediments generally consists of a mixture of marine autochthonous OC and laterally transported terrestrial OC. Marine OC (OC_{marine}) is predominantly delivered to the deep ocean via vertical settling, whereas OC_{terr} undergoes cross-shelf transport, lateral redistribution, and repeated reworking before final burial (Müller and Suess, 1979; Hedges and Keil, 1995; Burdige, 2007; Yin et al., 2024). As a result, the composition and apparent age structure of OC_{terr} are particularly sensitive to variations in source-area erosion and transport pathways. Distinguishing different OC_{terr} components is therefore essential for understanding their contrasting behaviors during transport and burial in deep-sea depositional systems. OC_{terr} can be separated into two components: biospheric OC ($OC_{terr\text{-}bio}$) derived from fresh vegetation and soil organic matter, and petrogenic OC (OC_{petro}) sourced from the weathering of ancient sedimentary rocks (Hilton et al., 2008; Lin et al., 2020; Zheng et al., 2017, 2024). Although OC_{petro} is widely regarded as an important component of the geologically inert carbon pool in the land-ocean system (Berner et al., 1983; Blair et al., 2003; Clark et al., 2013; Cui et al., 2016a; Blattmann et al., 2018), existing studies have primarily focused on modern sediments from nearshore and estuarine settings worldwide, where terrestrial inputs dominate (Hilton et al., 2011; Lin et al., 2020; Kim et al., 2023; Tao et al., 2023). Consequently, the glacial–interglacial evolution of OC_{petro}, and the extent to which it preserves source-area signals during cross-shelf transport and deep-sea burial, remain poorly constrained.

Against this background, the deep-water marginal basin of the northeastern South China Sea (NESCS) provides an ideal setting to investigate glacial–interglacial OC burial dynamics. The South China Sea (SCS), the largest marginal sea in the western Pacific, is particularly sensitive to climatic and oceanographic forcing owing to its unique geographic configuration, high sediment supply and accumulation (Wang et al., 2014; Liu et al., 2016; Li et al., 2018). The Luzon Strait, the sole deep-water gateway connecting the SCS with the Pacific Ocean, plays a pivotal role in regional material and energy exchange (Qu et al., 2006). The NESCS is characterized by a well-defined source-to-sink system, receiving sediments from the Pearl River, Taiwan, and Luzon. Among these sources, Taiwan represents a major contributor of OC_{petro} due to active tectonics and intense physical erosion, providing favorable conditions for disentangling OC_{terr} components (Kao et al., 2006b; Blattmann et al., 2018, 2019; Lin et al., 2024). Moreover, sedimentary records from this region are highly sensitive to East Asian monsoon (EAM) variability and glacial–interglacial sea-level fluctuations, and continuous deposition enables the recovery of high-resolution records spanning orbital to millennial timescales. Variations in the western Pacific boundary current (the Kuroshio) may further influence sedimentary processes indirectly by modulating regional hydrographic conditions (Wang et al., 2018; Tong et al., 2023; Bertaz et al., 2024; Zheng et al., 2024).

Previous studies have shown that in continental margins and deep-water sedimentary systems, the $\Delta^{14}C$ of sedimentary OC commonly integrate information on source carbon age together with cross-shelf transport times, resuspension-redeposition processes, and reservoir effects (Mollenhauer et al., 2005; Bao et al., 2018). As such, $\Delta^{14}C$ can be used to assess residence times associated with transport and recycling of OC from different sources. N/C and stable carbon isotopes ($\delta^{13}C$) have also been demonstrated to provide robust constraints on the relative contributions of $OC_{terr\text{-}bio}$ and OC_{petro}, and thus serve as effective tracers for endmember identification (Hilton et al., 2010). In addition, the association between OC and mineral surfaces in sedimentary systems may systematically record variations in transport pathways, recycling intensity, and preservation efficiency, offering further insight into process controls on deep-water OC burial.

Here, we investigate sediment Core S04 from the NESCS (Fig. 1). We combine measurements of TOC, total nitrogen (TN), $\delta^{13}C$, mean grain size (Mz), specific surface area (SSA), radiocarbon isotopes, and lignin phenols with a three-endmember mixing model based on TN/TOC and $\delta^{13}C$. $\Delta^{14}C$ and OC loading (OC/SSA) are further employed as

process-sensitive constraints. This integrated approach allows us to systematically examine the evolution of OC burial across glacial–interglacial cycles and to assess how climatic forcing and sedimentary processes jointly regulate OC burial in a deep-water marginal basin.

alt-text: Fig. 1

Fig. 1

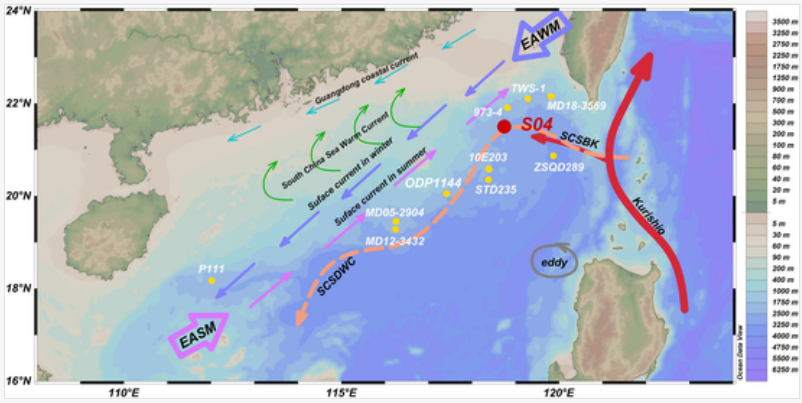

Overview map of the study area and Core S04
The map illustrates the major atmospheric and oceanic circulation systems in the South China Sea, including the EASM (magenta hollow arrows) and EAWM (purple hollow arrows), the Kuroshio and its South China Sea Branch (red arrows; Shen et al., 2022), the South China Sea Deep Water Current (orange dashed arrows; Qu et al., 2006; Liu et al., 2010), and the South China Sea Warm Current (green curved arrows; Liu et al., 2010). Surface circulation patterns during winter (purple arrows) and summer (magenta arrows) are shown following Wang et al. (2020). The cyclonic eddy northwest of Luzon Island is indicated by a grey oval (Liu et al., 2011; Zhang et al., 2023). (For interpretation of the references to color in this figure legend, the reader is referred to the Web version of this article.)

2 Regional setting

The South China Sea (SCS) is located in the western tropical to subtropical Pacific Ocean and is a semi-enclosed deep-sea basin surrounded by landmasses, including Luzon Island to the east, the Indochina Peninsula to the west, Malaysia and Borneo to the south, and southern China and Taiwan Island to the north (Zheng et al., 2016, Fig. 1). Water exchange between the SCS and western Pacific occurs through the Luzon Strait, showing a “sandwich structure” with inflow in upper and deep layers and outflow in intermediate layers (Zheng et al., 2023). Surface circulation in the SCS exhibits pronounced seasonal variability. During winter, cyclonic circulation prevails under the influence of the cold and dry East Asian Winter Monsoon (EAWM), whereas in summer, the warm and humid East Asian Summer Monsoon (EASM) drives anticyclonic circulation (Wang et al., 2014; Chen et al., 2023; Tong et al., 2023).

NESCS hosts a complex current system comprising the NE-SW-oriented Guangdong Coastal Current (GCC), the year-round northeastward South China Sea Warm Current (SCSWC, originating from eastern Guangdong's coastal and offshore deep waters), and the South China Sea Deep Water Current (SCSDWC) (Liu et al., 2016; Shen et al., 2022; Tong et al., 2023). The South China Sea Branch of the Kuroshio (SCSBK) intrudes through the Luzon Strait, critically modulating regional circulation, nutrient conditions, primary productivity, and biogeochemical cycling of carbon and Q4 nitrogen (Wang et al., 2018a; Tong et al., 2023).

3 Samples and methods

3.1 Core S04

Core S04 is located on the continental slope of the NESCS (118°45.4′E, 21°30.2′N, water depth 2446 m below sea level, Fig. 1) and was obtained in September 2020 by the research vessel Dongfanghong 3, with a core length of 448 cm. It was dissected longitudinally and divided into 448 samples at 1-cm intervals and lyophilized separately. Core S04 is a homogeneous grey-black silt, with brown and grey-black silt interbedded with clayey silt in the upper section from 0 to 188 cm, and the lower section 188–448 cm is dominated by clayey silt with occasional silt and sandy silt, with no sedimentary discontinuity (Fig. 2).

alt-text: Fig. 2

Fig. 2

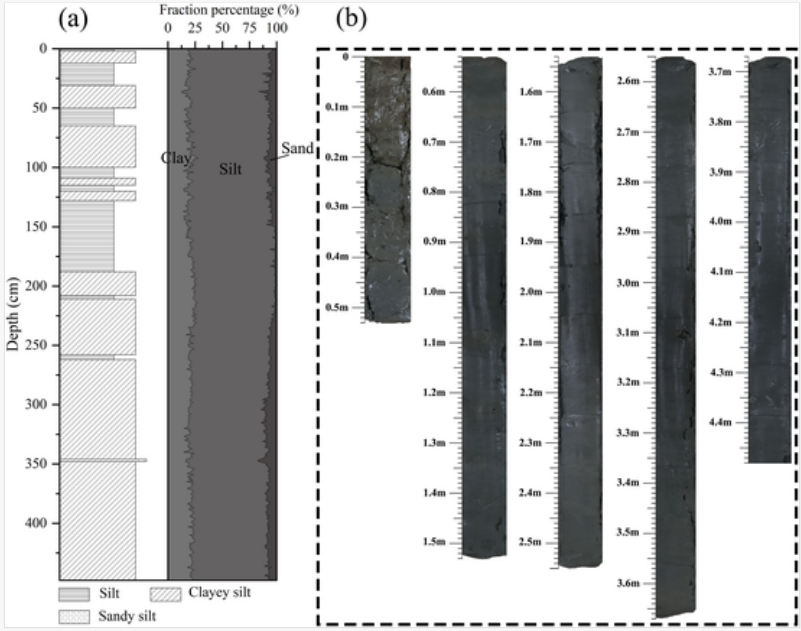

(a) Lithologic and grain-size composition and (b) scanning photographs of sediments from Core S04.

3.2 Chronology and age-depth modeling

11 sediment samples were selected from Core S04 for radiocarbon dating to reconstruct the chronological framework. More than 10 mg of planktonic foraminifer *Globigerinoides ruber* with of shell diameters >63 μm was selected from each sample. AMS ^{14}C analyses were completed at the Institute of Geochemistry Chinese Academy of Sciences, and the results obtained were converted to calibrated ages using the Calib 8.20 software (Stuiver and Reimer, 2016) with the Marine 20 calibration database (Heaton et al., 2020). Bayesian analysis using the Bacon software was applied to build an age-depth model for the Core S04 (Table A1), the age of the carbon reservoir used for the calculation $\Delta R = -135 \pm 47$ yr (Luo et al., 2023).

3.3 Sediment physical properties

3.3.1 Grain size

0.1 g of each sample (n = 448) was taken at 1-cm intervals, treated with 1 M HCl and 15% NaOH to remove carbonate and organic material, and dispersed with 1 M sodium hexametaphosphate. The treated samples were tested using a Mastersizer 2000 laser diffraction particle sizer to obtain grain size, with a repeat measurement error of ≤ ±3%.

3.3.2 Specific surface area (SSA)

SSA was determined following Waterson and Canuel (2008). A total of 1 g of each sample was taken at 2-cm intervals into glass vials respectively (n = 224) and heated in a muffle furnace at 350 ℃ for 12 h to remove organic material from the samples. SSA was then measured using an automatic nitrogen adsorption analyzer (BSD-PS4, Bestdo Instruments, China) via the five-point BET method, with repeated measurement errors < ±3%.

3.4 Bulk geochemical parameters

3.4.1 TOC, TN and $\delta^{13}C$

TOC, TN, and $\delta^{13}C$ were analyzed at the Third Institute of Oceanography, Ministry of Natural Resources (MNR), China. The samples were taken at 2-cm intervals (n = 224), freeze-dried, and homogenized by grinding to pass through a 100-mesh sieve (<150 μm). Approximately 1 g of each sample was treated with 1 M HCl to remove inorganic carbon, washed to neutrality, freeze-dried, and re-ground. The treated samples were analyzed using a Thermo Flash 2000 elemental analyzer interfaced with a MAT 253 isotope ratio mass spectrometer. $\delta^{13}C$ composition is reported relative to the VPDB standard using the following equation (Hsu et al., 2014):

$$\delta^{13}C\ (‰) = \left(R_{sample}/R_{VPDB}\ \text{-}1\right) \times 1000 \quad (1)$$

where R_{sample} and R_{VPDB} are the ratios of $^{13}C/^{12}C$ in the sample and the standard, respectively. Based on the repeated measurements of international reference materials, the precision of TOC and TN measurements is ±0.02 wt% and

±0.002 wt%, respectively, while the precision of $\delta^{13}C$ analysis is better than ±0.2‰.

3.4.2 Radiocarbon (^{14}C) analysis and expression

Follow the method described by Ausín et al. (2023), 12 sediment samples were selected for radiocarbon (^{14}C) analysis. Samples were pretreated following the same procedure as for TOC analysis: inorganic carbon was removed with 1 M HCl, washed with deionized water until neutral, and freeze-dried. The treated samples were measured for $^{14}C/^{12}C$ ratios using an accelerator mass spectrometer (AMS). The radiocarbon content of TOC is reported as the fraction of modern carbon (Fm), relative to the ^{14}C abundance of atmospheric CO_2 in 1950 CE. Isotopic fractionation during sample preparation and measurement was corrected using the measured $\delta^{13}C$ values.

3.5 Lignin phenols

Lignin was analyzed by a modified method based on the conventional alkaline CuO oxidations method described by Yu et al. (2011). About 1 g of 100-mesh (<150 μm) sediment was accurately weighed together with 1 g of CuO and 0.05 g of Fe $(NH_4)_2(SO_4)_2 \cdot 6H_2O$ in a Teflon reaction vessel, and 10 mL of 2 M NaOH was added in a glove box filled with N_2. The Teflon reaction vessel was then placed in a reactor and heated for 3 h at 170 °C. After cooling to room temperature, the recovered standards (ethyl vanillin and trans-cinnamic acid) were added to the alkaline solution. The mixed solution was transferred to a centrifuge tube with 15 mL of 1 M NaOH, the supernatant was collected, and the solution was adjusted to pH = 1 using 6 M HCl. The sample was extracted using a Cleanert PEP-SPE column (500 mg, Agela Technologies), eluted with ethyl acetate, blown dry under nitrogen, and redissolved in acetonitrile. The resulting solution was mixed with bis-trimethylsilyl-trifluoroacetamide and 1% trimethylchlorosilane (BSTFA+1% TMCS) and derivatized at 60 °C for 1 h. Lignin phenols in the derivatized solutions were analyzed using a Thermo Fisher 1300 gas chromatograph (GC) equipped with a flame ionization detector (FID).

Lignin phenols used as molecular proxies included three vanillyl phenols (vanillin, acetovanillone, and vanillic acid), three syringyl phenols (syringaldehyde, acetosyringone, and syringic acid), three *p*-hydroxy phenols (*p*-hydroxybenzaldehyde, *p*-hydroxyacetophenone, and *p*-hydroxybenzoic acid) and two cinnamyl phenols (*p*-coumaric and ferulic acids). Lignin concentration is expressed as Σ_8 (mg/10 g dry weight), calculated as the sum of S + V + C, and normalizing to 100 mg OC gives Λ_8 (mg/100 mg OC) (~~Hedges and Mann,1979~~Hedges and Mann, 1979; Tareq et al., 2004). The concentration of each lignin oxidation product was calculated using an internal calibration curve based on a single lignin-phenol standard. The standard curves for all target compounds showed excellent linearity within the analytical concentration range ($R^2 > 0.999$).

3.6 Three endmembers mixing model

The use of TOC/TN together with the $\delta^{13}C$ to constrain organic matter sources has been widely applied in studies of continental shelf and deep-sea sedimentary environments (Yu et al., 2010; Zhang et al., 2014; Bi et al., 2015; Wang et al., 2020; Jeong et al., 2023; Liu et al., 2023; Li et al., 2024). OC derived from different sources differs systematically in photosynthetic pathways, organic matter composition, and sensitivity to early diagenetic alteration, resulting in distinguishable TOC/TN and $\delta^{13}C$ signatures (Hedges et al., 1997; Meyers, 1997; Hilton et al., 2010).

Given that OC in the study area is primarily composed of marine autochthonous material and terrigenous inputs, and that multiple regional provenance studies based on clay mineral assemblages, Sr-Nd isotopes, and rare earth element (REE) compositions consistently identify Taiwan as the dominant source of terrigenous detrital material to the NESCS (Liu et al., 2017; Wang et al., 2020; Bertaz et al., 2024), OC burial in Core S04 sediments was partitioned into three endmembers: marine OC (OC_{marine}), terrestrially derived biospheric OC from Taiwan ($OC_{terr\text{-}bio}$), and rock-derived OC originating from the weathering of Taiwanese bedrock (OC_{petro}).

The three endmembers mixing model based on a Monte Carlo simulation was applied to semi-quantitatively estimate the relative contributions of different OC sources. The model uses TN/TOC ratios and $\delta^{13}C$ values as source tracers (Hilton et al., 2010; Andersson, 2011; Hu et al., 2014; Li et al., 2017). All calculations were performed in Matlab (2023). It is expressed as:

$$TN/TOC_{terr\text{-}bio} \times f_{terr\text{-}bio} + TN/TOC_{petro} \times f_{petro} + TN/TOC_{marine} \times f_{marine} = TN/TOC_{sample} \quad (2)$$

$$\delta^{13}C_{terr\text{-}bio} \times f_{terr\text{-}bio} + \delta^{13}C_{petro} \times f_{petro} + \delta^{13}C_{marine} \times f_{marine} = \delta^{13}C_{sample} \quad (3)$$

$$f_{terr\text{-}bio} + f_{petro} + f_{marine} = 1 \quad (4)$$

Where $f_{terr\text{-}bio}$, f_{petro} and f_{marine} represent the relative contributions of $OC_{terr\text{-}bio}$, OC_{petro} and OC_{marine}, respectively; TN/TOC_{sample} and $\delta^{13}C_{sample}$ are the measured parameters of bulk sediment samples. Compared with TOC/TN, the ratio form TN/TOC shows higher sensitivity to variations in OC_{terr} endmembers and was therefore adopted as a model constraint (Perdue and Koprivnjak, 2007).

Endmember TN/TOC and $\delta^{13}C$ values were compiled from published measurements of representative source materials from the study area and adjacent regions (Table 1). For each endmember, literature-reported mean values and standard deviations were used to describe natural variability. These parameters were incorporated as probabilistic constraints in the Monte Carlo simulations. Details of endmember uncertainty evaluation are provided in the Supplementary Material (Text A1).

alt-text: Table 1

Table 1

The table layout displayed in this section is not how it will appear in the final version. The representation below is solely purposed for providing corrections to the table. To view the actual presentation of the table, please click on the Preview located at the top of the page.

TN/TOC and $\delta^{13}C$ of endmembers.

OC Sources	TN/TOC (Average ± SD)	$\delta^{13}C$ (‰, Average ± SD)	References
marine phytoplankton	0.182 ± 0.003	−20.3 ± 1.7	Wei et al. (2020); Lin et al. (2024)
bedrock from western Taiwan	0.184 ± 0.009	−24.8 ± 2	Kao et al., 2000; Hilton et al. (2010)
terrestrial biosphere in forested catchments of Taiwan	0.06 ± 0.05	−26 ± 1	Hilton et al. (2010)

3.7 Statistical analyses

All statistical analyses were performed using Origin 2023. Normality of continuous variables was assessed using the Shapiro-Wilk test. For group comparisons, independent-samples *t* tests were applied when data were normally distributed and variances were homogeneous (Levene's test, $p > 0.05$). Welch's *t*-test was used when the assumption of equal variances was violated. When data did not meet normality assumptions, the Mann–Whitney *U* test was applied.

Correlation analyses were conducted using Pearson correlation analysis when both variables were normally distributed; otherwise, Spearman rank correlation coefficients were used. All statistical tests were two-tailed, and statistical significance was evaluated at $p < 0.05$ or $p < 0.01$.

4 Results

4.1 Chronology and sediment characteristics

Core S04 has a bottom boundary age of 36.5 ka and spans from MIS 3 to the Holocene, covering major cold climate events such as Heinrich events (H), the Last Glacial Maximum (LGM), and the Younger Dryas (YD). Sediment accumulation rates in Core S04 are generally low, ranging from 5.08 to 59.32 cm/ka, with an average of 18.68 cm/ka, and rates since the Holocene are generally higher than during the last glacial period (Fig. 3).

Images may appear blurred during proofing as they have been optimized for fast web viewing. A high quality version will be used in the final publication. Click on the image to view the original version.

alt-text: Fig. 3

Fig. 3

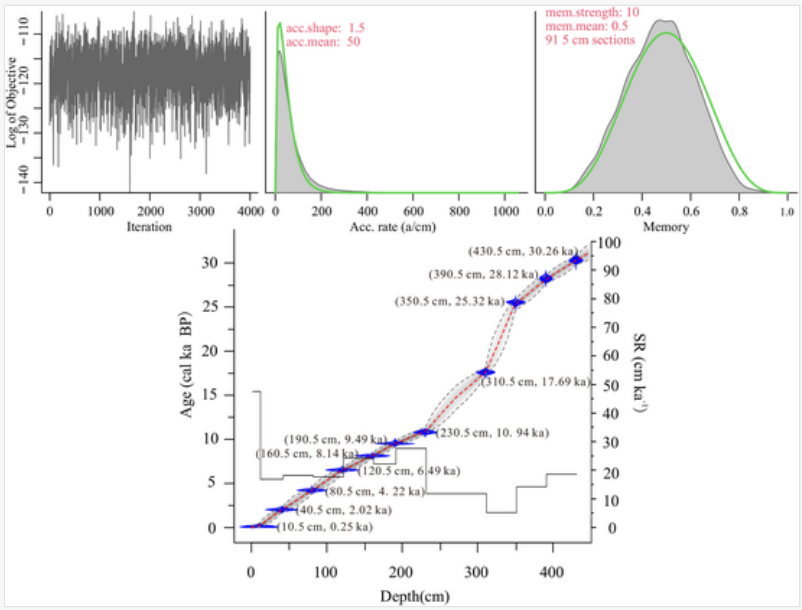

Bayesian age-depth model of Core S04
The upper three panels depict the iterations: (left panel) good runs show a stationary distribution with little structure among neighbouring iterations, the prior (green curves) and posterior (grey histograms) distributions for the (middle panel) accumulation rate, and (right panel) memory. Bottom panel shows the calibrated ^{14}C dates (blue) and the age-depth model and the sedimentation rate with depth variation (solid black line). The red curve shows the single 'best' model based on the mean age for each depth; grey stippled lines show 95% confidence intervals. (For interpretation of the references to color in this figure legend, the reader is referred to the Web version of this article.)

The sediments are mainly composed of silt (60.48%–82.68%), with a secondary clay content (12.53%–27.70%) and a smaller amount of sand (0.72%–17.50%) (Fig. 2a). Mz of the sediments ranges from 7.24 to 18.32 μm, with a mean value of 10.735 ± 1.659 μm (Fig. 4d). During the glacial period, Mz increases and then decreases, reaching a minimum at the end of the YD cold event, and generally increased during the Early Holocene, with a low value around 5 ka. The SSA of Core S04 varied between 8.97 and 21.20 m^2/g (mean 15.70 ± 2.70 m^2/g, Fig. A2b). SSA gradually increased since 32 ka, decreased at the end of the LGM, and has fluctuated on millennial scales since the Holocene.

Images may appear blurred during proofing as they have been optimized for fast web viewing. A high quality version will be used in the final publication. Click on the image to view the original version.

alt-text: Fig. 4

Fig. 4

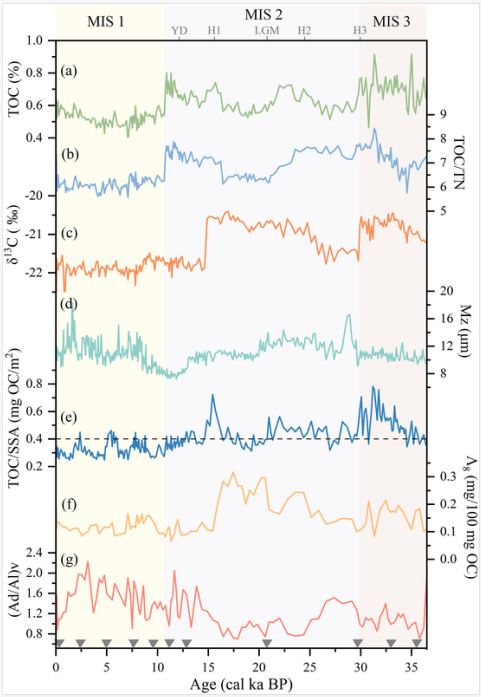

Multi-proxy variations in Core S04 spanning MIS 1–3. From top to bottom, panels show (a) TOC contents; (b) TOC/TN ratios; (c) $\delta^{13}C$ values; (d) Mz; (e) TOC/SSA; (f) Λ_8 contents; and (g) $(Ad/Al)_V$. MIS 1–3 are indicated by subtle background shading for stratigraphic reference. Major cold intervals during MIS 2, including the YD, H1, LGM, H2, and H3, are labeled at the top of the

figure. Grey inverted triangles represent radiocarbon-dated horizons, and the black dotted line indicates a TOC/SSA value of 0.4 mg OC m^{-2}.

Replacement Image: FIG4.tif

Replacement Instruction: We have uploaded a revised version of Figure 4 to correct a minor formatting error. In the original figure, there was an extra space in the unit label δ13C (‰); this has now been corrected. Please use the new file. Thank you.

4.2 Bulk organic matter characteristics

The TOC content in Core S04 sediments ranged from 0.389% to 0.915% (mean 0.603% ± 0.095%, Fig. 4a), and the TN content ranged from 0.061% to 0.134% (mean 0.090% ± 0.009%, Fig. A2a), showing similar downcore trends. Correlation analysis reveals a significant positive relationship between TOC and TN ($R^2 = 0.657$, $p < 0.01$, Fig. A1), indicating that both parameters share a common source. TOC/TN varied between 5.57 and 8.43 (Fig. 4b), with a mean value of 6.70 ± 0.64, and are generally higher during the glacial than during the interglacial period. $\delta^{13}C$ values range from −23.414‰ to −20.396‰ (Fig. 4c), with a mean value of −21.409 ± 0.572‰. $\delta^{13}C$ becomes more negative around the end of H1and remains relatively stable during the Holocene.

Radiocarbon analyses show that the fraction modern (Fm) values are consistently far below the modern standard (Table A2). Fm values range from 0.0476 to 0.2273 (mean 0.1127 ± 0.0613), corresponding to apparent ^{14}C ages of 11.9–24.5 ka BP. All samples exhibit strongly negative $\Delta^{14}C$ values, ranging from −952.4 ‰ to −772.7 ‰ (mean −885.2 ± 57.1‰), indicating a dominant contribution from ^{14}C-depleted, pre-aged OC. The $\Delta^{14}C$ record shows clear temporal variability. The most negative $\Delta^{14}C$ values (<−949‰) occur at ~16.5 ka, suggesting a maximum contribution of old carbon. In contrast, $\Delta^{14}C$ values during the Holocene are less negative (−773‰ to −818‰), indicating a relative increase in younger carbon components.

4.3 Lignin phenols and degradation indicators

The Σ_8 and Λ_8 records of Core S04 show generally consistent trends and a strong positive correlation ($R^2 = 0.85$, $p < 0.01$; Fig. A3a). Σ_8 values range from 0.046 to 0.180 mg/10 g ds (dry sediment), with a mean value of 0.089 ± 0.036 mg/10 g ds (Fig. A2c), whereas Λ_8 values ranged from 0.065 to 0.317 mg/100 mg OC, with a mean value of 0.148 ± 0.055 mg/100 mg OC (Fig. 4f). Both parameters increased since 30 ka, remain relatively high between 25 and 16.5 ka, then decreased rapidly and remain at relatively low and stable values since 15.5 ka. Higher Σ_8 indicates substantial input from terrestrial vascular plants, while elevated Λ_8 reflects a higher proportion of lignin in TOC, highlighting the dominant influence of OC_{terr}.

The S/V and C/V ratios serve as indicators of lignin source composition, reflecting contributions from different plant groups. The S/V and C/V range from 0.64 to 1.65 and from 0.24 to 1.07, respectively, with mean values of 1.11 ± 0.21 and 0.61 ± 0.21 (Figs. A2f and g), and show a positive correlation ($R^2 = 0.48$, $p < 0.01$; Fig. A3b). Before H1, lower S/V and C/V ratios indicate dominance of gymnosperm-derived lignin. After 16.5 ka, both ratios increase, suggesting enhanced angiosperms input. Around 8 ka, S/V decreases while C/V remains relatively stable, likely reflecting complex environmental changes during the transition from deglaciation to the mid-Holocene.

The acid-aldehyde ratios $(Ad/Al)_V$ and $(Ad/Al)_S$ are used to characterize the degradation or humification state of lignin tissues. Since vanillyl phenols are present in all vascular plants, $(Ad/Al)_V$ is more sensitive to oxidative degradation than $(Ad/Al)_S$ (Gordon and Goñi, 2003; Cui et al., 2016a). $(Ad/Al)_V$ range from 0.65 to 2.23 (mean 1.28 ± 0.36; Fig. 4g), and $(Ad/Al)_S$ range from 0.35 to 1 (mean 0.67 ± 0.10; Fig. A2d). The variations of both ratios show a positive correlation ($R^2 = 0.17$, $p < 0.01$; Fig. A3c). $(Ad/Al)_V$ reaches its minimum during the LGM and gradually increases after 16.5 ka, with a temporary decrease during the short deglaciation–early Holocene transition. High ratios indicate enhanced oxidative degradation of lignin. DHBA/V is often used as a proxy of relative soil OC versus vascular plant contribution (Cui et al., 2016a). DHBA/V values in Core S04 sediments range from 0.263 to 0.798 (mean 0.480 ± 0.131; Fig. A2e). Lower values, particularly from the onset of H3 to the end of H1, suggest greater contribution from fresh plant debris, whereas the increasing trend since H1 indicates enhanced soil-derived OC_{terr} input.

4.4 Source apportionment of organic carbon

Based on sedimentary TN/TOC ratios and $\delta^{13}C$ signatures, the three endmembers mixing approach was applied to Core S04 to semi-quantitatively assess the relative contributions of OC_{marine}, $OC_{terr\text{-}bio}$, and OC_{petro} (Fig. 5). Considering the natural variability of endmember compositions and the potential influence of early diagenetic processes on bulk geochemical proxies, the results are interpreted in terms of relative changes rather than absolute source proportions.

will be used in the final publication. Click on the image to view the original version.

alt-text: Fig. 5

Fig. 5

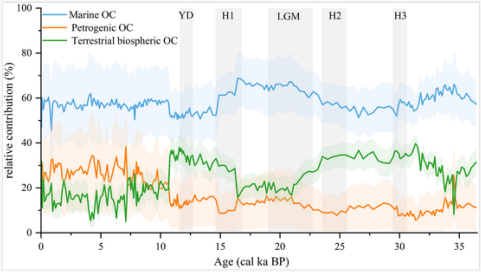

Temporal variations in the relative contributions of marine, petrogenic, and biospheric OC in Core S04. The OC_{marine}, OC_{petro}, and $OC_{terr\text{-}bio}$ components are shown by blue, orange, and green lines, respectively. Shaded bands of the same colors represent the corresponding uncertainty envelopes (mean ± 1σ) derived from endmember variability. The grey rectangles indicate cold-event periods. (For interpretation of the references to color in this figure legend, the reader is referred to the Web version of this article.)

During the early part of the record (MIS 3), OC_{marine} remained relatively high but showed a significant declining trend. Over the same interval, the relative contribution of $OC_{terr\text{-}bio}$ increased, whereas OC_{petro} remained low with only minor fluctuations. With the transition into the last glacial period, OC_{marine} increased progressively and persisted at elevated levels. In contrast, $OC_{terr\text{-}bio}$ decreased markedly, while OC_{petro} showed only a slight increase and remained a minor component, indicating a relative weakening of the biospheric fraction within the terrestrial endmember.

From H1 onward, the relative contribution of OC_{marine} declined from its preceding high values and followed a broadly continuous downward trend. At the same time, $OC_{terr\text{-}bio}$ increased and reached comparatively higher levels. OC_{petro} also increased during this interval but decreased during cold-event phases (H1 and YD), reflecting pronounced adjustments in the internal structure of OC_{terr} sources.

During the Holocene, OC_{marine} remained relatively high but varied within a limited range. In contrast, the terrestrial endmember continued to evolve internally, characterized by a progressive decline in the relative importance of $OC_{terr\text{-}bio}$ and sustained, moderately variable contributions from OC_{petro}. Overall, the three endmembers exhibit structural adjustments under a generally stable background during this period.

Taken together, the three endmembers mixing model results reveal clear orbital-to millennial-scale variability in OC sources at Core S04, expressed by alternating phases of strengthened and weakened relative importance of OC_{marine}, together with persistent adjustments in both the overall influence and internal composition of OC_{terr} inputs.

5 Discussion

5.1 Decoupling between source composition and radiocarbon age of sedimentary OC

In deep-sea sedimentary systems, bulk geochemical proxies that record OC source information may also be influenced by post-depositional diagenetic alteration and recycling. Therefore, before interpreting variations in OC sources and radiocarbon ages, it is necessary to evaluate the relative importance of these processes over the timescales considered. In Core S04, variations in TN/TOC and $\delta^{13}C$ do not covary with changes in the degree of degradation indicated by terrestrial lignin degradation and compositional parameters, but instead display clear stage-dependent patterns (Fig. 4g; Fig. 5). Combined with the high sensitivity of $\delta^{13}C$ to OC source differences and its consistency with the established provenance framework of the study area (Liu et al., 2017; Wang et al., 2020; Bertaz et al., 2024), these results indicate that, at millennial- and orbital-scale timescales, bulk geochemical indices primarily reflect changes in OC source structure rather than dominant post-depositional alteration (Goñi et al., 1998; Zhu et al., 2011).

The three endmembers mixing model based on TN/TOC and $\delta^{13}C$ shows that the relative contributions of OC_{marine}, $OC_{terr\text{-}bio}$, and OC_{petro} in Core S04 exhibit clear but non-synchronous temporal evolution (Fig. 5). Although the overall OC pool reflects combined marine and adjacent terrestrial inputs, the magnitude and direction of change differ among OC types across climatic stages, implying distinct sensitivities to climate and sedimentary conditions.

Radiocarbon data further clarify the nature of these differences. Although S04 samples plot mainly between the marine OC and Taiwan-derived terrestrial petrogenic OC endmembers in TN/TOC–$\delta^{13}C$ space, $\Delta^{14}C$ values do not follow a single mixing trajectory (Fig. 6). Samples closer to terrestrial endmembers often show higher (less negative) $\Delta^{14}C$ values, whereas samples with more marine-like compositions tend to exhibit lower (more negative) $\Delta^{14}C$ values. This pattern indicates that OC source composition and radiocarbon age are not linked by a simple linear relationship.

Images may appear blurred during proofing as they have been optimized for fast web viewing. A high quality version will be used in the final publication. Click on the image to view the original version.

alt-text: Fig. 6

Fig. 6

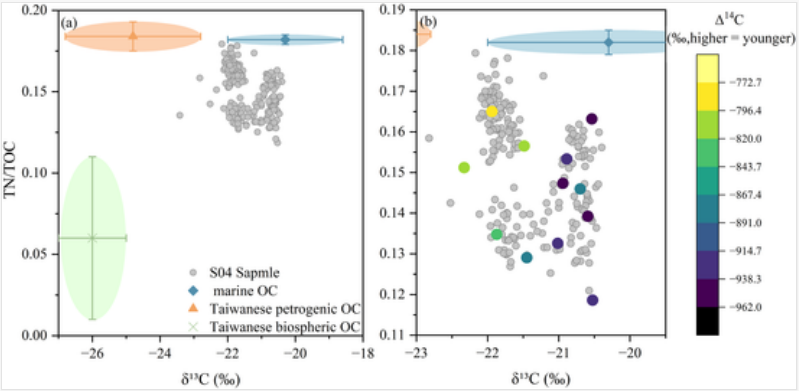

(a) TN/TOC versus $\delta^{13}C$ diagram showing Core S04 samples relative to marine, Taiwanese petrogenic, and Taiwanese biospheric OC endmembers (means ± variability). (b) Zoom-in view of the S04 sample cluster, with symbols colored by measured $\Delta^{14}C$ values (higher, less negative values indicate younger carbon).

Previous studies have shown that, in deep continental-margin settings, $\Delta^{14}C$ is highly sensitive to cross-shelf transport, resuspension–redeposition, and recycling timescales, whereas $\delta^{13}C$ and TN/TOC more directly reflect OC composition and provenance (Goñi et al., 1998; Mollenhauer et al., 2005; Bao et al., 2018). In regions such as the NESCS, the high erosion rate of the Taiwan orogenic belt, short source–sink distance, and frequent high-energy runoff events facilitate the mixing and recycling of OC of different ages in the shelf–deep-water system, thereby further amplifying the decoupling characteristics between source composition and radiocarbon age (Blair and Aller, 2012; Bao et al., 2018, 2020). These observations indicate that OC burial in the S04 deep-water system is not governed by a single process through time, but by a hierarchy of controls that adjusts with changing climate boundary conditions. Accordingly, the strength of "process control" is not constant but varies with sea-level state and monsoon background.

At glacial–interglacial timescales, sea-level fluctuations and EAM variability jointly define the primary climatic framework governing OC burial in the NESCS. Their influence is expressed through changes in OC source inputs as well as through reorganization of cross-shelf transport and recycling pathways (Zheng et al., 2016; Zhang et al., 2022). Together, these factors determine the extent of reworking experienced by OC before it reaches the deep-water sink, thereby modulating the relative importance of process control on final burial characteristics. The ratio of OC to mineral surface area (TOC/SSA), as a process-based indicator of OC loading, directly reflects the amount of OC preserved per unit mineral surface and provides an effective link between OC sources, transport dynamics, and final preservation (Keil et al., 1994; Ashfaq et al., 2025).

Based on this framework, we combine source indicators ($\delta^{13}C$, TN/TOC) with process indicators ($\Delta^{14}C$, TOC/SSA) to examine OC burial during three characteristic climate intervals—MIS 3, MIS 2, and MIS 1. This approach allows a systematic assessment of how process control modulates, and at times dominates, the final burial state of deep-water OC under contrasting climatic conditions.

5.2 MIS 3 (36.5–30 ka): a dynamic background state of deep-sea OC burial

MIS 3 exhibits unique climatic conditions distinct from typical glacial and interglacial periods, featuring relatively mild mean states accompanied by millennial-scale variability (Dannenmann et al., 2003; Zhang et al., 2014, 2023). During 36.5–30 ka, TOC contents in Core S04 remained relatively high (around 0.7%) and fluctuated frequently. These variations show no significant correlation with Mz ($p > 0.05$), indicating that OC burial during this interval was not primarily controlled by local hydrodynamic conditions, but instead reflects the combined influence of regional-scale inputs and transport processes.

With respect to OC_{terr}, global sea level during MIS 3 was approximately 100 m lower than present but exhibited relatively modest variability (Spratt and Lisiecki, 2016), favoring sustained delivery of terrestrial material. In Core S04, increasing trends in C/N ratios, the persistent presence of lignin signals (Λ_8 averaging 0.161 mg/100 mg OC), and an increase in the relative contribution of $OC_{terr\text{-}bio}$ (Fig. 7b–d, f) indicate that terrestrial organic matter continuously contributed to the deep-sea OC pool and exerted a stable influence on its composition. Similar trends have been reported from other regional sediment cores (e.g., Core 973-4; Wang et al., 2020). During this interval, SSA shows a slight decreasing trend, whereas TOC/SSA increases from ~0.4 to ~0.8 mg OC m^{-2} (Fig. 7c) and correlates positively with the proportion of $OC_{terr\text{-}bio}$ ($R^2 = 0.31$, $p < 0.01$, Fig. A3d). This pattern indicates a progressive increase in OC loading on the mineral surfaces. Together with persistent lignin signatures and low oxidation indices, these results

suggest that $OC_{terr\text{-}bio}$ retained relatively high reactivity during transport and deposition, enhancing its stabilization through association with fine-grained mineral surfaces. This mechanism implies a gradual adjustment in OC preservation pathways under relatively stable TOC levels and is consistent with the preferential mineral binding of biospheric OC enriched in polar functional groups (Keil et al., 1994; Arnarson and Keil, 2007).

alt-text: Fig. 7

Fig. 7

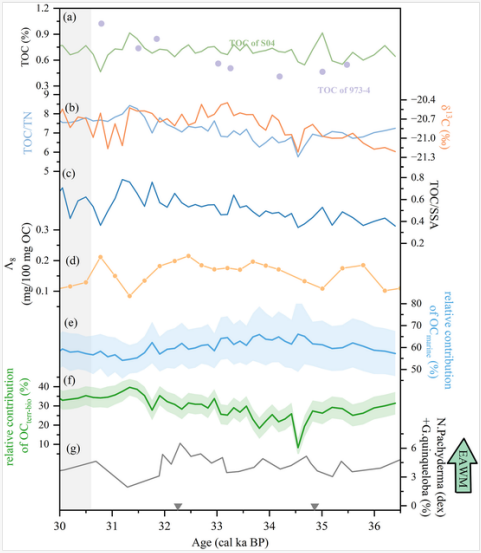

Changes in OC proxies and climatic background recorded in Core S04 before 30 ka BP. (a) TOC of Core S04 and Core 973-4 (Wang et al., 2020); (b) TOC/TN and $\delta^{13}C$; (c) TOC/SSA; (d) Λg; (e-f) relative contributions of OC_{marine} and $OC_{terr\text{-}bio}$; (g) EAWM index (Xiang et al., 2009). Grey inverted triangles represent radiocarbon-dated horizons, and the grey shaded band marks the H3.

In terms of OC_{marine}, a strengthened EAWM during late MIS 3, together with relatively warm sea-surface temperatures, likely enhanced upper-ocean mixing and promoted nutrient supply to surface waters, creating favorable conditions for marine primary productivity (Steinke et al., 2010; Dai et al., 2013; Tong et al., 2023). However, the relative contribution of OC_{marine} in Core S04 does not show a corresponding increase (Fig. 7e). This pattern does not necessarily imply a reduction in the absolute flux of OC_{marine}; instead, it more likely reflects redistribution among OC sources, in which enhanced terrestrial contributions "dilute" the relative marine signal rather than reduced its absolute flux.

Notably, radiocarbon data from MIS 3 already show partial decoupling between $\Delta^{14}C$ ages and OC compositional indicators (Fig. 6): when $\Delta^{14}C$ values are strongly negative, the bulk OC composition remains dominated by marine characteristics. This suggests that cross-shelf transport and recycling processes exerted a strong influence on the OC age structure during this interval. Radiocarbon ages are highly sensitive to minor inputs of pre-aged OC, whereas compositional indicators such as $\delta^{13}C$ respond more weakly to the same processes. Moreover, recycled aged OC contributing to $\Delta^{14}C$ depletion does not necessarily exhibit strongly depleted $\delta^{13}C$ values typical of terrestrial biospheric endmembers, but instead often falls within marine or mixed compositional ranges (Blair and Aller, 2012; Mollenhauer et al., 2005; Bao et al., 2018, 2020). As a result, even modest inputs of recycled OC_{terr} can significantly affect $\Delta^{14}C$ without producing a resolvable shift in $\delta^{13}C$.

Overall, MIS 3 can be defined as a "dynamic background state" of OC burial. Under relatively gentle low sea-level conditions, the source-to-sink framework remained stable, and deep-sea OC burial occurred within a marine-dominated system that was persistently modulated by terrestrial inputs, particularly biospheric components. These terrestrial contributions were progressively stabilized through mineral association, enhancing burial stability. This background state provides a clear reference against which the shifts in dominant controls observed during MIS 2 and MIS 1 can be evaluated.

5.3 MIS 2 (30–10.6 ka): transport intensification and monsoon modulation under low sea level

MIS 2 represents the glacial–deglacial transition phase, characterized by pronounced sea-level changes, reaching its lowest point approximately 130 m below modern values during the LGM (Spratt and Lisiecki, 2016). The shift from widespread shelf exposure to progressive inundation fundamentally adjusted the geometric structure and hydrodynamic

structure of the shelf–deep-sea system, creating strongly time-dependent conditions for sediment transport, temporary storage, and recycling (Li et al., 2018; Zhang et al., 2022; Ashfaq et al., 2025; Chen et al., 2025).

Compared with MIS 3, the early to middle MIS 2 interval (30–16.5 ka) is marked by a significant increase in Mz ($p < 0.05$), while SSA shows no statistically significant change (Fig. 8b; Fig. A2b). During this period, both TOC contents and OC/SSA values decline markedly (Fig. 8c–f; $p < 0.05$). This combination indicates inhibited OC loading under conditions of relatively stable mineral carrier supply. Previous studies show that under high-energy transport, rapid cross-shelf transfer, and strong particle sorting, OC is difficult to effectively combine with mineral surfaces or may be stripped off during recycling, leading to reduced OC/SSA values (Mayer, 1994; Blair and Aller, 2012; Bao et al., 2018). Consistent with this interpretation, lignin Σ_8 and Λ_8 values in Core S04 increase significantly ($p < 0.05$), while $(Ad/Al)_V$ and DHBA/V ratios remain low (Fig. 8d and e), indicating enhanced inputs of vascular plant-derived OC with comparatively limited oxidative degradation. Together, these features indicate that during the glacial period the deep-water system operated under a physically filtered regime dominated by high-energy, rapid transport. Organic matter was efficiently delivered to deep water but lacked sufficient residence time for stable mineral association, resulting in kinetically limited OC loading (Goñi et al., 1998; Blair and Aller, 2012; Keil and Mayer, 2004; Bao et al., 2018).

alt-text: Fig. 8

Fig. 8

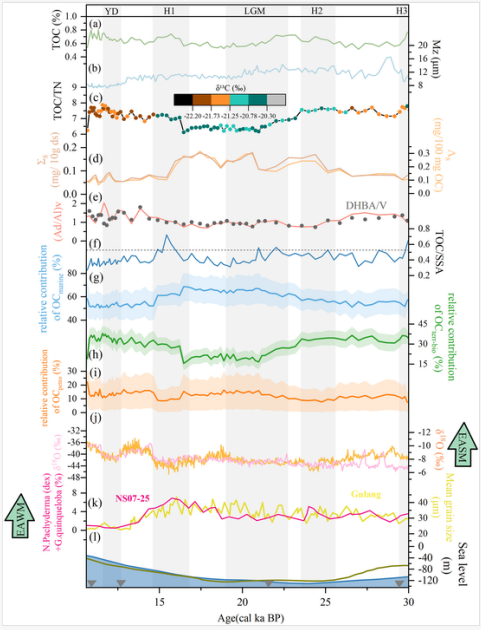

Changes in OC proxies and climatic background recorded in Core S04 during MIS 2. (a) TOC; (b) Mz; (c) TOC/TN and $\delta^{13}C$; (d) Σ_8 and Λ_8; (e) degradation indices; (f) TOC/SSA; (g–i) relative contributions of OC_{marine}, OC_{petro} and $OC_{terr\text{-}bio}$; (j) EASM index (pink line, ~~North Greenland Ice Core Project Members~~North Greenland Ice Core Project members, 2004; orange line, Cheng et al., 2016); (k)

EAWM index (magenta line, Xiang et al., 2009; yellow line, Sun et al., 2012); and (l) sea level (Spratt and Lisiecki, 2016, pink line; Zhang et al., 2022, Khaki line). Grey inverted triangles represent radiocarbon-dated horizons, and the grey shaded band marks the cold event. (For interpretation of the references to color in this figure legend, the reader is referred to the Web version of this article.)

These processes are also reflected in changes in OC source composition. Relative to MIS 3, $OC_{terr\text{-}bio}$ decreases significantly between 30 and 16.5 ka, while the relative contribution of OC_{petro} increases (Fig. 8h and i; $p < 0.05$), although it remains a minor component overall. This pattern indicates structural redistribution within the OC_{terr} pool. Under rapid cross-shelf transport and energetic re-sorting, chemically stable, mineral-associated OC_{petro} is more likely to survive along the source-to-sink pathway, whereas more reactive $OC_{terr\text{-}bio}$ is preferentially lost during transport and early diagenesis (Blair and Aller, 2012; Blattmann et al., 2019). At the same time, the relative contribution of OC_{marine} increases (Fig. 8g). This trend reflects both enhanced marine productivity supported by stronger EAWM conditions and nutrient availability over the exposed shelf (Higginson et al., 2003; He et al., 2013; Tong et al., 2023), and the selective removal of reactive OC_{terr}, which passively amplifies the marine signal in relative terms.

Under this background of rapid transport and efficient burial, $\Delta^{14}C$ ages in Core S04 are generally younger than during MIS 3. This pattern likely reflects faster transfer from source regions to the depositional sink, which reduced opportunities for mixing with aged carbon pools and extensive recycling (Mollenhauer et al., 2005; Bao et al., 2018). Increased relative contributions of young OC_{marine} may have provided a secondary influence on this trend.

After ~16.5 ka, rising sea level progressively inundated the continental shelf and reintegrated it into the marine transport system, leading to a fundamental shift in shelf–deep-sea dynamics. Compared with glacial conditions, Σ_8 and Λ_8 values decrease rapidly and remain low (Fig. 8d), while S/V, C/V, $(Ad/Al)_V$, and DHBA/V ratios increase significantly (Fig. 8e; Figs. A2f and g). These changes indicate a shift in OC_{terr} sources toward angiosperms and deeper soil and bedrock material (Bao et al., 2017), consistent with increased precipitation, intensified erosion, and vegetation reorganization driven by strengthening EASM conditions during deglaciation (Zheng et al., 2024; Huang et al., 2025). A pronounced increase in SSA reflects enrichment of fine-grained mineral carriers in deep-sea sediments ($p < 0.05$), whereas further declines in OC/SSA indicate reduced OC loading per unit mineral surface area (Fig. 8f; Fig. A2b). Unlike the glacial period, the decrease in OC/SSA is not due to limitations in loading dynamics, but more likely reflects the dilution effect of increasing mineral surface area. These patterns indicate a transition from a transport-dominated system to one characterized by fine-grained accumulation and enhanced resuspension–redeposition. In this setting, the continental shelf increasingly functioned as an intermediate reservoir, extending the residence time and recycling pathways of OC prior to final burial. This mechanism has been widely recognized as a key driver of older apparent radiocarbon ages in deep-sea sediments (Mollenhauer et al., 2005; Bao et al., 2020). During the H1 event, Core S04 records a short-lived but pronounced increase in OC/SSA (Fig. 8f), indicating rapid adjustment of OC loading. This increase is not accompanied by enhanced lignin concentrations or systematically older $\Delta^{14}C$ ages, suggesting that neither OC_{terr} input nor recycling duration increased substantially. Instead, a slight rise in TOC combined with a modest decrease in SSA points to short-term particle reorganization and re-sorting (Fig. 8a; Fig. A2b). The OC/SSA peak during H1 therefore most likely reflects transient hydrodynamic restructuring rather than a stable state imposed by long-term boundary conditions.

Between 16.5 and 10.6 ka, as the EAWM weakened and the EASM strengthened (Fig. 8j and k), the relative contribution of OC_{marine} declined, while $OC_{terr\text{-}bio}$ increased significantly (Fig. 8g and h; $p < 0.05$). OC_{petro} shows no further systematic increase. These changes indicate redistribution among reactive OC pools rather than continued enrichment of OC_{petro}. Consistent with this pattern, $\Delta^{14}C$ ages trend older, reflecting the growing influence of prolonged transport pathways and enhanced recycling on the radiocarbon signal.

Overall, variations in deep-water OC during MIS 2 were primarily governed by sea-level-driven shifts in transport and preservation regimes. Between 30 and 16.5 ka, extremely low sea level promoted high-energy transport and strong particle sorting, producing pronounced process filtering and selective preservation. After ~16.5 ka, rising sea level and enhanced recycling shifted the system toward a mode dominated by fine-particle accumulation and surface-area dilution effects.

5.4 MIS 1(Since 10.6ka): background-state modulation under high sea level

MIS 1 corresponds to the Holocene warm period, during which sea level rose to and remained near its present highstand. Widespread inundation of the continental shelf re-established the shelf as a major intermediate reservoir and processing zone, substantially weakening the extensive cross-shelf resuspension and redistribution that characterized glacial conditions (Cathalot et al., 2013; Heijnen et al., 2022; Gan et al., 2022).

The most notable features of this stage include markedly reduced TOC contents (Fig. 9a; $p < 0.05$), a significant increase in Mz ($p < 0.05$), and persistently low OC loading, which remains stable at very low values (Fig. 9e; <0.4 mg OC m^{-2}). Notably, OC/SSA shows no significant correlation with either $OC_{terr\text{-}bio}$ or OC_{petro}, but displays a weak yet significant negative correlation with OC_{marine} ($R^2 = 0.07$, $p < 0.05$). This decoupling indicates that, unlike the deglacial stage where OC/SSA declined mainly due to surface-area expansion and dilution, the Holocene deep-water OC system entered a low-loading steady state controlled by persistent resuspension and oxidative reworking. Under this regime,

newly formed OC–mineral associations are continuously disrupted, and the rate of OC binding remains lower than the rates of oxidation and stripping (Hartnett et al., 1998; Keil et al., 2004; Burdige, 2005; Blair and Aller, 2012). As a result, the influence of source input proportions on OC/SSA is systematically suppressed, producing a clear source–loading decoupling.

alt-text: Fig. 9

Fig. 9

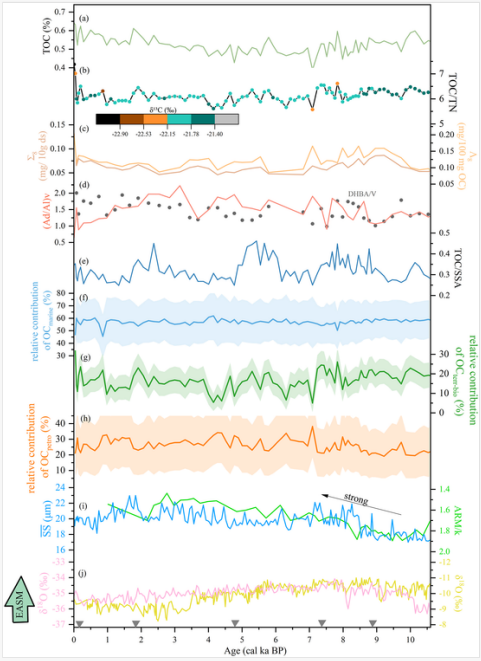

Changes in OC proxies and climatic background recorded in Core S04 during MIS 1. (a) TOC; (b) TOC/TN and $\delta^{13}C$; (c) Σ_8 and Λ_8; (d) degradation coefficient; (e) TOC/SSA; (f–h) relative contributions of OC_{marine}, OC_{petro} and $OC_{terr\text{-}bio}$; (i) bottom-water intensity of Core S04 and 10E203 (Zheng et al., 2016); (j) EASM index (pink line, ~~North Greenland Ice Core Project Members~~North Greenland Ice Core Project members, 2004; orange line, Cheng et al., 2016). Grey inverted triangles represent the dating layers. (For interpretation of the references to color in this figure legend, the reader is referred to the Web version of this article.)

Sedimentary dynamic indicators provide direct support for this interpretation. An increase in sortable silt mean size ($\overline{SS}$) indicates sustained and strong bottom-current activity in the study area during the Holocene (methods in Text A2). Under such conditions, sediment particles experience long transport pathways and repeated resuspension–redeposition before reaching the deep-sea sink. These processes preferentially remove fine particles and substantially reduce OC loading on mineral surfaces through hydrodynamic sorting and hydraulic filtering. Similar mechanisms have been identified in Holocene records from other marginal seas (Goñi et al., 1998; Blair and Aller, 2012; Bao et al., 2018).

Within this "rapid-transit–intense-reworking" framework, changes in OC source composition should be understood as the result of strong reprocessing rather than as primary drivers. Although intensified EASM conditions during the Holocene enhanced erosion of deeper soils and bedrock in Taiwan, increasing OC_{terr} supply to the system (Zheng et al., 2024; Huang et al., 2025), reworking under strong bottom-current control exerted a pronounced selective preservation effect. Lignin parameters provide independent constraints: Σ_8 and Λ_8 values are generally low, whereas $(Ad/Al)_V$ and DHBA/V ratios are elevated (Fig. 9c and d), indicating weakened vascular plant signatures and more extensive recycling and degradation of OC_{terr}. These patterns agree with previous observations from Holocene shelf systems, where biospheric components are preferentially retained upstream and more inert fractions become relatively enriched offshore (Goñi et al., 1998; Blair and Aller, 2012; Bao et al., 2017).

Radiocarbon results show that sedimentary OC during MIS 1 is overall younger, indicating that high sea level strengthened shelf trapping of terrestrial particles and substantially shortened cross-shelf recycling pathways relative to glacial conditions. Consequently, OC entering the deep-sea system experienced shorter transport times (Mollenhauer et al., 2005; Bao et al., 2018). Importantly, this reduced transport and residence time does not contradict the strong oxidative degradation inferred from lignin proxies. Instead, the Holocene deep-water system likely reflects a mode of high-intensity oxidation over short timescales. Under strong bottom currents, particles are transported relatively rapidly into deep water but undergo frequent resuspension and repeated exposure to well-oxygenated waters or surface sediments, allowing substantial chemical alteration to occur within limited time intervals. Accordingly, even with

relatively high proportions of OC_{petro} (Fig. 9h), $\Delta^{14}C$ values remain comparatively young, reinforcing the conclusion that radiocarbon signals primarily record transport and recycling timescales rather than simple source mixing ratios.

In summary, deep-water organic carbon burial during MIS 1 is characterized by a low-loading steady state maintained by strong bottom currents and prolonged reworking under high sea level. The final preservation state is dominated by transport and recycling processes and shows a markedly weak response to variations in source input.

5.5 Integration of multi-stage controls and a multi-scale climate framework for OC burial

Synthesis of the MIS 3, MIS 2, and MIS 1 discussions shows that deep-water OC burial in the NESCS exhibits clear stage-dependent controls on glacial–interglacial timescales. The dominant mechanisms shift systematically with changes in source–sink configuration and sedimentary dynamic conditions (Fig. 10).

alt-text: Fig. 10

Fig. 10

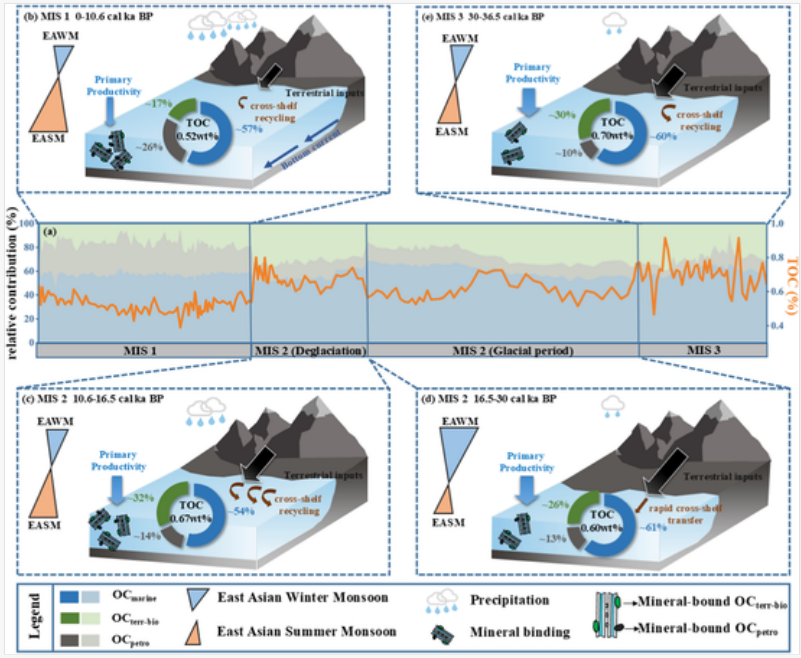

Conceptual model illustrating the evolution of deep-water OC burial in the NESCS. (a) Temporal evolution of TOC and the relative contributions of different organic carbon types in Core S04 over the past ~36.5 kyr. The orange curve indicates changes in TOC content, and the stacked color bands show variations in the relative composition of OC_{marine} (blue), OC_{petro} (grey), and $OC_{terr\text{-}bio}$ (green). (b–e) The main controlling factors for OC burial in the NESCS during three Marine Isotope Stages. (For interpretation of the references to color in this figure legend, the reader is referred to the Web version of this article.)

During MIS 3 (Fig. 10e), relatively stable low sea level maintained sustained shelf–basin connectivity, allowing OC to reach the deep basin within a comparatively steady transport framework. OC_{marine} dominated the input, while $OC_{terr\text{-}bio}$ exerted a persistent secondary influence. The deep-water system thus operated as a "dynamic background state," in which source signals were transmitted to the sedimentary record with limited overprinting. In early–middle MIS 2 (30–16.5 ka, Fig. 10d), extremely low sea level profoundly restructured the source–sink system. Rapid cross-shelf transport and strong particle sorting became dominant. Under high-energy conditions, OC–mineral association was strongly constrained, leading to marked reductions in OC/SSA and TOC. Deep-water records from this interval primarily reflect physical sorting and process filtering under energetic transport, rather than changes in source input, with OC preservation tightly limited by kinetic conditions.

Following the onset of deglaciation (late MIS 2, after ~16.5 ka, Fig. 10c), rapid sea-level rise restored the shelf as an intermediate reservoir. Fine particles accumulated along the shelf–slope transition, and recycling intensified. Compared with the glacial period, transport energy weakened, but the apparent residence time of OC increased substantially. As a result, OC/SSA remained low while $\Delta^{14}C$ ages became older, indicating a transition to a recycling-dominated, low-loading regime in the deep basin. During the Holocene (Fig. 10b), high sea level further reduced broad shelf–basin connectivity. Although intensified EASM conditions favored OC_{terr} supply, strong bottom-current control, long transport pathway lengths, repeated resuspension, and oxidative reworking continued to suppress OC loading. Consequently, the deep-water system evolved toward a steady operational state with a weak response to variations in source input.

These stage-dependent differences indicate that source-related signals ($\delta^{13}C$ and TN/TOC) and process-related signals ($\Delta^{14}C$ and OC/SSA) in deep-water sedimentary systems are not independent (Blair and Aller, 2012). Instead, they respond to climate forcing with different weights. Source indicators primarily record "what enters the system," whereas process indicators more directly reflect "what the organic carbon experiences" during cross-shelf transport, resuspension, and mineral association. Shifts in their relative importance provide the fundamental explanation for the decoupling or partial recoupling between OC composition and radiocarbon age observed across different stages (Goñi et al., 1998; Bao et al., 2018).

These source–sink processes and their dominant controls do not occur independently but are embedded within a broader ocean–atmosphere climate system. As the principal upper-ocean circulation linking the western Pacific and the SCS, the Kuroshio Current and its branches may have experienced changes in strength and pathway on glacial–interglacial timescales, with the potential to modulate upper-ocean thermal structure and nutrient availability (Qu et al., 2006; Wan and Jian, 2014; Wang et al., 2018). However, in the deep-water environment represented by Core S04, effective OC preservation depends primarily on transport pathway lengths, resuspension frequency, and opportunities for mineral association prior to final burial. These factors are mainly governed by sea-level-controlled shelf–basin connectivity and monsoon-driven sedimentary dynamics. In contrast, the Kuroshio mainly acts on the upper ocean and must pass through multiple filters—including biological production, vertical export, cross-shelf transport, and depositional reworking—before reaching the sedimentary sink (Hedges and Keil, 1995; Qu et al., 2006; Burdige, 2007). As a result, its influence is readily integrated or attenuated by stronger first-order controls associated with sea-level reorganization and monsoon-driven sediment dynamics (Blum and Hattier-Womack, 2009; Blair and Aller, 2012). At the temporal scale and depositional setting considered here, the Kuroshio therefore functions as a background modulator rather than a primary driver of stage-scale variations in deep-water OC burial.

At longer temporal and broader spatial scales, regional monsoon variability is inherently embedded within the global atmospheric circulation system (Haug et al., 2001; Koutavas and Lynch-Stieglitz, 2004; McGee et al., 2014). Under the current sedimentation rates and sampling resolution of Core S04, the record most clearly captures climate forcing at orbital to millennial timescales. Higher-frequency variability, such as ENSO, may influence source-area hydroclimate and erosion regimes, but its signal is strongly time-averaged during cross-shelf transport, repeated resuspension, and pre-burial reworking, limiting its expression as a distinct sedimentary response (Zhao et al., 2016). In contrast, latitudinal migration of the Intertropical Convergence Zone (ITCZ), as a low-frequency background process, exerts systematic control on EAM intensity and seasonality, thereby influencing regional precipitation patterns, catchment erosion, and terrestrial material export to the ocean (Wang et al., 2001; Cheng et al., 2016; Clemens et al., 2018). Accordingly, variations in OC_{terr} input recorded in Core S04—such as systematic shifts in lignin parameters and $OC_{terr\text{-}bio}$ across the deglacial–Holocene transition—are more plausibly interpreted as responses to monsoon adjustment under changing global–tropical climate backgrounds, rather than as direct imprints of high-frequency climate events.

In summary, deep-water OC burial in the NESCS reflects a source–sink response system constrained stepwise by climate forcing across multiple scales. At orbital timescales, sea-level change restructures shelf–basin connectivity and sets the fundamental framework for OC transport and preservation. Within this framework, millennial-scale EAM variability modulates material input and sedimentary dynamics. Local processes including cross-shelf transport, hydrodynamic sorting, resuspension, and mineral protection ultimately determine OC storage state, loading efficiency, and apparent age. Deep-water sedimentary systems therefore act not as passive recorders of climate forcing, but as dynamic carbon sinks that integrate and selectively filter external signals across different temporal scales.

6 Conclusion

Based on a multi-proxy analysis of deep-water Core S04 from the NESCS, this study identifies the dominant controls on OC burial since the last glacial period and clarifies the stage-dependent evolution of its storage state. The results show that deep-water OC burial is governed by both the nature of organic matter inputs and, more importantly, by the structure of the source–sink system, sedimentary dynamics, and mineral protection processes.

1. Orbital-scale sea-level change defines the fundamental framework for OC transport, storage, and recycling by restructuring shelf–basin connectivity, while millennial-scale EAM variability modulates erosion, sedimentary energy, and background productivity. Within this framework, the OC that eventually enters the deep-water sediment reservoir is mainly determined by hydrodynamic sorting, selective degradation, and mineral surface binding processes, rather than a simple amplification of the source signal.

2. OC/SSA records the outcome of interactions between OC and mineral carriers during cross-shelf transport and reworking, integrating the effects of sedimentary energy, hydrodynamic sorting, and mineral protection. Variations in OC/SSA across climate stages therefore reflect selective modification of source signals, rather than a direct mapping of source-area changes.

3. In deep-water marginal-sea settings, $\Delta^{14}C$ is highly sensitive to transport pathway length, resuspension frequency, and recycling intensity, and primarily records the apparent residence time of OC rather than

its source end-member proportions. This highlights the need to interpret OC provenance together with transport and reworking processes.

Overall, this study proposes a sea-level architecture–monsoon input–process filtering framework, highlighting deep marginal basins as active carbon sinks that selectively transform and stabilize OC across climate states. These findings refine current understanding of deep-water carbon burial along continental margins and provide a process-based perspective for evaluating the stability of marginal-sea carbon sinks under climate change.

Q6 Uncited references

Hedges and Mann, 1979; North Greenland Ice Core Project members, 2004

CRediT authorship contribution statement

Xiao Huang: Formal analysis, Investigation, Writing - original draft. Xinqing Zou: Funding acquisition, Project administration, Writing - review and editing. Zhuoyue Zhang: Methodology, Software. Yadi Zhou: Methodology. Chuchu Zhang: Methodology, Writing - review and editing. Xuejiao Jiang: Writing - review and editing. Chendong Ge: Supervision, Writing - review and editing. Ruxi Dou: Methodology. Yue Xue: Supervision. Chenglong Wang: Funding acquisition, Project administration, Writing - review and editing.

Declaration of competing interest

The authors declare that they have no known competing financial interests or personal relationships that could have appeared to influence the work reported in this paper.

Acknowledgement

The work was supported by the Natural Science Foundation of China (Grant No. 42106056), the State Key Laboratory Q5 of Marine Geology, Tongji University (No. MGK202410). We gratefully acknowledge Cruise NORC2020-05, carried out by the R/V Dongfanghong 3 in the South China Sea in May 2020, for providing the sediment samples used in this study.

Appendix A Supplementary data

Supplementary data to this article can be found online at https://doi.org/10.1016/j.quascirev.2026.109925.

References

The corrections made in this section will be reviewed and approved by a journal production editor. The newly added/removed references and its citations will be reordered and rearranged by the production team.

Andersson, A., 2011. A systematic examination of a random sampling strategy for source apportionment calculations. Sci. Total Environ. 412, 232–238. doi:10.1016/j.scitotenv.2011.10.031.

Arnarson, T.S., Keil, R.G., 2007. Changes in organic matter-mineral interactions for marine sediments with varying oxygen exposure times. Geochem. Cosmochim. Acta 71, 3545–3556. doi:10.1016/j.gca.2007.04.027.

Ashfaq, M.F., Zhao, B., Chen, L.L., Ding, Y., Wang, N., Ye, X.W., Gao, C., Duan, X.Y., Yao, P., 2025. Impacts of sea level rise and climate change on the sources, preservation and thermal stability of sedimentary organic carbon in the East China Sea inner shelf since the last deglaciation. Quat. Sci. Rev. 362, 109416. doi:10.1016/j.quascirev.2025.109416.

Ausín, B., Bossert, G., Krake, N., Paradis, S., Haghipour, N., de Madron, X.D., Alonso, B., Eglinton, T., 2023. Sources and fate of sedimentary organic matter in the Western Mediterranean Sea. Glob. Biogeochem. Cycles 37, e2023GB007695. doi:10.1029/2023GB007695.

Bao, H.Y., Kao, S.J., Lee, T.Y., Zehetner, F., Huang, J.C., Chang, Y.P., Lu, J.T., Lee, J.Y., 2017. Distribution of organic carbon and lignin in soils in a subtropical small mountainous river basin. Geoderma 306, 81–88. doi:10.1016/j.geoderma.2017.07.011.

Bao, R., Blattmann, T.M., 2020. Radiocarbonscapes of sedimentary organic carbon in the East Asian Seas. Front. Mar. Sci. 7, 517. doi:10.3389/fmars.2020.00517.

Bao, R., Uchida, M., Zhao, M.X., Haghipour, N., Montlucon, D., McNichol, A., Wacker, L., Hayes, J.M., Eglinton, T.I., 2018. Organic carbon aging during across-shelf transport. Geophys. Res. Lett. 45, 8425–8434. doi:10.1029/2018GL078904.

Bereiter, B., Eggleston, S., Schmitt, J., Nehrbass, A.C., Stocker, T.F., Fischer, H., Kipfstuhl, S., Chappellaz, J., 2015. Revision of the EPICA Dome C CO2 record from 800 to 600 kyr before present. Geophys. Res. Lett. 42, 542–549. doi:10.1002/2014GL061957.

Berner, R.A., Lasaga, A.C., Garrels, R.M., 1983. The carbonate-silicate geochemical cycle and its effect on atmospheric carbon dioxide over the past 100 million years. Am. J. Sci. 283, 641–683. doi:10.2475/ajs.283.7.641.

Bertaz, J., Liu, Z.F., Colin, C., Dapoigny, A., Lin, A.T.S., Li, Y.L., Jian, Z.M., 2024. Climatic and environmental impacts on the sedimentation of the SW Taiwan Margin since the last deglaciation: geochemical and mineralogical investigations. Paleoceanogr. Paleoclimatol. 39, 8. doi:10.1029/2023PA004745.

Bi, L., Yang, S.Y., Li, C., Guo, Y.L., Wang, Q., Liu, J.T., Yin, P., 2015. Geochemistry of river-borne clays entering the East China Sea indicates two contrasting types of weathering and sediment transport processes. G-cubed 16, 3034–3052. doi:10.1002/2015GC005867.

Blair, N.E., Aller, R.C., 2012. The fate of terrestrial organic carbon in the Marine environment. Ann. Rev. Mar. Sci 4, 401–423. doi:10.1146/annurev-marine-120709-142717.

Blair, N.E., Leithold, E.L., Ford, S.T., Peeler, K.A., Holmes, J.C., Perkey, D.W., 2003. The persistence of memory: the fate of ancient sedimentary organic carbon in a modern sedimentary system. Geochem. Cosmochim. Acta 67, 63–73. doi:10.1016/S0016-7037(02)01043-8.

Blattmann, T.M., Liu, Z., Zhang, Y., Zhao, Y., Haghipour, N., Montluçon, D.B., Plötze, M., Eglinton, T.I., 2019. Mineralogical control on the fate of continentally derived organic matter in the ocean. Science 366, 742–745. doi:10.1126/science.aax5345.

Blattmann, T.M., Zhang, Y., Zhao, Y., Wen, K., Lin, S., Li, J., Wacker, L., Haghipour, N., Plötze, M., Liu, Z., Eglinton, T.I., 2018. Contrasting fates of petrogenic and biospheric carbon in the South China Sea. Geophys. Res. Lett. 45, 9077–9086. doi:10.1029/2018GL079222.

Blum, M.D., Hattier-Womack, J., 2009. Climate change, sea-level change, and fluvial sediment supply to deepwater depositional systems. In: External Controls on Deep-Water Depositional Systems, 92. doi:10.2110/sepmsp.092.015.

Brovkin, V., Ganopolski, A., Archer, D., Munhoven, G., 2012. Glacial CO2 cycle as a succession of key physical and biogeochemical processes. Clim. Past 8, 251–264. doi:10.5194/cp-8-251-2012.

Burdige, D.J., 2005. Burial of terrestrial organic matter in marine sediments: a re-assessment. Glob. Biogeochem. Cycles 19, GB4011. doi:10.1029/2004GB002368.

Burdige, D.J., 2007. Preservation of organic matter in marine sediments: controls, mechanisms, and an imbalance in sediment organic carbon budgets? Chem. Rev. 107, 467–485. doi:10.1021/cr050347q.

Cartapanis, O., Bianchi, D., Jaccard, S.L., Galbraith, E.D., 2016. Global pulses of organic carbon burial in deep-sea sediments during glacial maxima. Nat. Commun. 7, 10796. doi:10.1038/ncomms10796.

Cartapanis, O., Galbraith, E.D., Bianchi, D., Jaccard, S.L., 2018. Carbon burial in deep-sea sediment and implications for oceanic inventories of carbon and alkalinity over the last glacial cycle. Clim. Past 14, 1819–1850. doi:10.5194/cp-14-1819-2018.

Cathalot, C., Rabouille, C., Tisnérat-Laborde, N., Toussaint, F., Kerhervé, P., Buscail, R., Loftis, K., Sun, M.Y., Tronczynski, J., Azoury, S., Lansard, B., Treignier, C., Pastor, L., Tesi, T., 2013. The fate of river organic carbon in coastal areas: a study in the Rhone River delta using multiple isotopic (δ13C, Δ14C) and organic tracers. Geochem. Cosmochim. Acta 118, 33–55. doi:10.1016/j.gca.2013.05.001.

Chen, F., Mao, S.Y., Zhou, W.Q., Li, G., Zhu, X.W., Yan, W., 2025. Organic matter burial and degradation in the southern South China Sea since the last glaciation. Global Planet. Change 248, 104771. doi:10.1016/j.gloplacha.2025.104771.

Chen, W., Zhang, R.H., Wu, R.G., Wen, Z.P., Zhou, L.T., Wang, L., Hu, P., Ma, T.J., Piao, J.L., Song, L., Wang, Z.B., Li, J.C., Gong, H.A., Huangfu, J.L., Liu, Y., 2023. Recent advances in understanding multi-scale climate variability of the Asian monsoon. Adv. Atmos. Sci. 40, 1429–1456. doi:10.1007/s00376-023-2266-8.

Cheng, H., Edwards, R.L., Sinha, A., Spotl, C., Yi, L., Chen, S.T., Kelly, M., Kathayat, G., Wang, X.F., Li, X.L., Kong, X.G., Wang, Y.J., Ning, Y.F., Zhang, H.W., 2016. The Asian monsoon over the past 640,000 years and ice age terminations. Nature 534, 640–646. doi:10.1038/nature18591.

Clark, K.E., Malhi, Y., New, M., Hilton, R.G., West, A.J., Gröcke, D.R., Bryant, C.L., Ascough, P.L., Caceres, A.R., 2013. New views on "old" carbon in the Amazon River: insight from the source of organic carbon eroded from the Peruvian Andes. G-cubed 14, 1644–1659. doi:10.1002/ggge.20122.

Clemens, S.C., Holbourn, A., Kubota, Y., Lee, K.E., Liu, Z., Chen, G., Nelson, A., Fox-Kemper, B., 2018. Precession-band variance missing from East Asian monsoon runoff. Nat. Commun. 9, 3364. doi:10.1038/s41467-018-05814-0.

Cui, X.Q., Bianchi, T.S., Jaeger, J.M., Smith, R.W., 2016a. Biospheric and petrogenic organic carbon flux along southeast Alaska. Earth Planet Sci. Lett. 452, 238–246. doi:10.1016/j.epsl.2016.08.002.

Cui, X.Q., Bianchi, T.S., Savage, C., Smith, R.W., 2016b. Organic carbon burial in fjords: terrestrial versus marine inputs. Deep Sea Res. Part A. Earth and Planetary Science Letters 451, 41–50. doi:10.1016/j.epsl.2016.07.003.

Dai, M.H., Cao, Z.M., Guo, X.H., Zhai, W.D., Liu, Z.Y., Yin, Z.Q., Xu, Y.P., Gan, J.P., Hu, J.Y., Du, C.J., 2013. Why are some marginal seas sources of atmospheric CO2? Geophys. Res. Lett. 40, 2154–2158. doi:10.1002/grl.50390.

Dannenmann, S., Linsley, B.K., Oppo, D.W., Rosenthal, Y., Beaufort, L., 2003. East Asian monsoon forcing of suborbital variability in the Sulu sea during marine Isotope stage 3: link to Northern Hemisphere climate. G-cubed 4, 1–13. doi:10.1029/2002GC000390.

Gan, Y.Q., De Almeida, F.N., Rossi, V.M., Steel, R.J., Olariu, C., 2022. Sediment transfer from shelf to deepwater slope: how does it happen? J. Sediment. Res. 92, 570–590. doi:10.2110/jsr.2021.013.

Goñi, M.A., Ruttenberg, K.C., Eglinton, T.I., 1998. A reassessment of the sources and importance of land-derived organic matter in surface sediments from the Gulf of Mexico. Geochem. Cosmochim. Acta 62, 3055–3075. doi:10.1016/S0016-7037(98)00217-8.

Hartnett, H.E., Keil, R.G., Hedges, J.I., Devol, A.H., 1998. Influence of oxygen exposure time on organic carbon preservation in continental margin sediments. Nature 391, 572–574. doi:10.1038/35351.

Haug, G.H., Hughen, K.A., Sigman, D.M., Peterson, L.C., Röhl, U., 2001. Southward migration of the intertropical convergence zone through the Holocene. Science 293, 1304–1308. doi:10.1126/science.1059725.

He, J., Zhao, M.X., Wang, P.X., Li, L., Li, Q.Y., 2013. Changes in phytoplankton productivity and community structure in the northern South China Sea during the past 260 ka. Palaeogeogr. Palaeoclimatol. Palaeoecol. 392, 312–323. doi:10.1016/j.palaeo.2013.09.010.

Heaton, T.J., Köhler, P., Butzin, M., Bard, E., Reimer, R.W., Austin, W.E.N., Ramsey, C.B., Grootes, P.M., Hughen, K.A., Kromer, B., Reimer, P.J., Adkins, J., Burke, A., Cook, M.S., Olsen, J., Skinner, L.C., 2020. Marine20—The marine radiocarbon Age calibration curve (0-55,000 cal BP). Radiocarbon 62, 779–820. doi:10.1017/RDC.2020.68.

Hedges, J.I., Keil, R.G., 1995. Sedimentary organic matter preservation: an assessment and speculative synthesis. Mar. Chem. 49, 81–115. doi:10.1016/0304-4203(95)00008-F.

Hedges, J.I., Keil, R.G., Benner, R., 1997. What happens to terrestrial organic matter in the ocean? Org. Geochem. 27, 195–212. doi:10.1016/S0146-6380(97)00066-1.

Hedges, J.I., Mann, D.C., 1979. The characterization of plant tissues by their lignin oxidation products. Geochem. Cosmochim. Acta 43, 1803–1807. doi:10.1016/0016-7037(79)90028-0.

Heijnen, M.S., Mienis, F., Gates, A.R., Bett, B.J., Hall, R.A., Hunt, J., Kane, I.A., Pebody, C., Huvenne, V.A., Soutter, E.L., Clare, M.A., 2022. Challenging the highstand-dormant paradigm for land-detached submarine canyons. Nat. Commun. 13, 3448. doi:10.1038/s41467-022-31114-9.

Higginson, M.J., Maxwell, J.R., Altabet, M.A., 2003. Nitrogen isotope and chlorin paleoproductivity records from the Northern South China Sea: remote vs. local forcing of millennial- and orbital-scale variability. Mar. Geol. 201, 223–250. doi:10.1016/S0025-3227(03)00218-4.

Hilton, R.G., Galy, A., Hovius, N., Chen, M.C., Horng, M.J., Chen, H.Y., 2008. Tropical-cyclone-driven erosion of the terrestrial biosphere from mountains. Nat. Geosci. 1, 759–762. doi:10.1038/ngeo333.

Hilton, R.G., Galy, A., Hovius, N., Horng, M.J., Chen, H., 2011. Efficient transport of fossil organic carbon to the ocean by steep mountain rivers: an orogenic carbon sequestration mechanism. Geology 39, 71–74. doi:10.1130/G31352.1.

Hilton, R.G., Galy, A., Hovius, N., Horng, M.J., Chen, H.E., 2010. The isotopic composition of particulate organic carbon in mountain rivers of Taiwan. Geochem. Cosmochim. Acta 74, 3164–3181. doi:10.1016/j.gca.2010.03.004.

Hsu, F.H., Su, C.C., Wang, C.H., Lin, S., Liu, J., Huh, C.A., 2014. Accumulation of terrestrial organic carbon on an active continental margin offshore southwestern Taiwan: Source-to-sink pathways of river-borne organic particles. J. Asian Earth Sci. 91, 163–173. doi:10.1016/j.jseaes.2014.05.006.

Hu, B.Q., Li, J., Zhao, J.T., Wei, H.L., Yin, X.J., Li, G.G., Liu, Y., Sun, Z.L., Zou, L., Bai, F.L., Dou, Y.G., Wang, L.B., Sun, R.T., 2014. Late Holocene elemental and isotopic carbon and nitrogen records from the East China Sea inner shelf: implications for monsoon and upwelling. Mar. Chem. 162, 60–70. doi:10.1016/j.marchem.2014.03.008.

Huang, C., Wu, L.Y., Cheng, J.S., Qu, X.X., Luo, Y.Y., Zhang, H.L., Ye, F., Wei, G.J., 2025. Sedimentary responses to climatic variations and Kuroshio intrusion into the northern South China Sea since the last deglaciation. Global Planet. Change 245, 104671. doi:10.1016/j.gloplacha.2024.104671.

Jeong, Y.J., Park, H.J., Baek, N., Seo, B.S., Lee, K.S., Kwak, J.H., Choi, S.K., Lee, S.M., Yoon, K.S., Lim, S.S., Choi, W.J., 2023. Assessment of sources variability of riverine particulate organic matter with land use and rainfall changes using a three-indicator ($\delta^{13}C$, $\delta^{15}N$, and C/N) Bayesian mixing model. Environ. Res. 216, 114653. doi:10.1016/j.envres.2022.114653.

Kao, S.J., Liu, K.K., 2000. Stable carbon and nitrogen isotope systematic in a human disturbed watershed (Lanyang-His) in Taiwan and the estimation of biogenic particulate organic carbon and nitrogen fluxes. Glob. Biogeochem. Cycles 14, 189–198. doi:10.1029/1999GB90007.

Kao, S.J., Roberts, A.P., Hsu, S.C., Chang, Y.P., Lyons, W.B., Chen, M.T., 2006a. Monsoon forcing, hydrodynamics of the Kuroshio current, and tectonic effects on sedimentary carbon and sulfur cycling in the Okinawa trough since 90 ka. Geophys. Res. Lett. 33. doi:10.1029/2005GL025154.

Kao, S.J., Shiah, F.K., Wang, C.H., Liu, K.K., 2006b. Efficient trapping of organic carbon in sediments on the continental margin with high fluvial sediment input off Southwestern Taiwan. Cont. Shelf Res. 26, 2520–2537. doi:10.1016/j.csr.2006.07.030.

Keil, R.G., Dickens, A.F., Arnarson, T., Nunn, B.L., Devol, A.H., 2004. What is the oxygen exposure time of laterally transported organic matter along the Washington margin? Mar. Chem. 92, 157–165. doi:10.1016/j.marchem.2004.06.024.

Keil, R.G., Montluçon, D.B., Prahl, F.G., Hedges, J.I., 1994. Sorptive preservation of labile organic matter in marine sediments. Nature 370, 549–552. doi:10.1038/370549a0.

Kim, D., Kim, J.H., Ahn, Y., Jang, K., Jung, J.Y., Bae, M., Nam, S.I., 2023. Large contributions of petrogenic and aged soil-derived organic carbon to Arctic fjord sediments in Svalbard. Sci. Rep. 13, 17935. doi:10.1038/s41598-023-45141-z.

Kohfeld, K.E., Ridgwell, A., 2009. Glacial-Interglacial variability in atmospheric CO2. Surface Ocean-Lower Atmosphere Processes 187, 251–286. doi:10.1029/2008GM000845.

Koutavas, A., Lynch-Stieglitz, J., 2004. Variability of the marine ITCZ over the eastern Pacific during the past 30,000 years. In: The Hadley Circulation: Present, past and Future. Advances in Global Change

Research, 21. pp. 347–369. doi:10.1007/978-1-4020-2944-8_13.

LaRowe, D.E., Arndt, S., Bradley, J.A., Estes, E.R., Hoarfrost, A., Lang, S.Q., Lloyd, K.G., Mahmoudi, N., Orsi, W.D., Walter, S.R.S., Steen, A.D., Zhao, R., 2020. The fate of organic carbon in marine sediments - new insights from recent data and analysis. Earth Sci. Rev. 204, 103146. doi:10.1016/j.earscirev.2020.103146.

Li, D.W., Chen, M.N., Liu, S., Zhang, H.L., Wang, Z.C., Ning, X.Y., Tian, J.W., Zhao, M.X., 2024. Continuous deposition of pre-aged organic carbon in the southern Mariana Trench since the last deglaciation. Chem. Geol. 662, 122212. doi:10.1016/j.chemgeo.2024.122212.

Li, M.K., Ouyang, T.P., Roberts, A.P., Heslop, D., Zhu, Z.Y., Zhao, X., Tian, C.J., Peng, S.S., Zhong, H.X., Peng, X.C., Qiu, Y., 2018. Influence of Sea level change and Centennial East Asian monsoon variations on Northern South China Sea sediments over the past 36 kyr. G-cubed 19, 1674–1689. doi:10.1029/2017GC007321.

Li, X.X., Zhang, Z.R., Wade, T.L., Knap, A.H., Zhang, C.L.L., 2017. Sources and compositional distribution of organic carbon in surface sediments from the lower Pearl River to the coastal South China Sea. J. Geophys. Res.: Biogeosciences 122, 2104–2117. doi:10.1002/2017JG003981.

Lin, B.Z., Liu, Z.F., Eglinton, T.I., Kandasamy, S., Blattmann, T.M., Haghipour, N., Huang, K.F., You, C.F., 2020. Island-wide variation in provenance of riverine sedimentary organic carbon: a case study from Taiwan. Earth Planet Sci. Lett. 539, 116238. doi:10.1016/j.epsl.2020.116238.

Lin, B.Z., Liu, Z.F., Eglinton, T.I., Wiesner, M.G., Blattmann, T.M., Haghipour, N., 2024. Organic carbon sources in surface sediments on the Northern South China Sea. J. Geophys. Res.: Biogeosciences 129, e2023JG007909. doi:10.1029/2023JG00790.

Liu, F., Yang, C.P., Chang, X.H., Liao, Z.W., 2017. Provenance discrimination of the last glacial sediments from the northeastern South China Sea and its paleoenvironmental indications. Terr. Atmos. Ocean Sci. 29, 131–148. doi:10.3319/TAO.2017.07.31.01.

Liu, J.G., Xiang, R., Chen, M.H., Chen, Z., Yan, W., Liu, F., 2011. Influence of the Kuroshio current intrusion on depositional environment in the Northern South China Sea: evidence from surface sediment records. Mar. Geol. 285, 59–68. doi:10.1016/j.margeo.2011.05.010.

Liu, S., Li, D.W., Xiang, R., Yu, M., Zhang, H.L., Li, L., Zhao, M.X., 2023. Intensification of the East Asian winter monsoon resulted in greater preservation of terrestrial organic carbon on the inner shelf of the East China Sea since the last 1400 years. Palaeogeogr. Palaeoclimatol. Palaeoecol. 615, 111454. doi:10.1016/j.palaeo.2023.111454.

Liu, Z.F., Colin, C., Li, X.J., Zhao, Y.L., Tuo, S.T., Chen, Z., Siringan, F.P., Liu, J.T., Huang, C.Y., You, C.F., Huang, K.F., 2010. Clay mineral distribution in surface sediments of the northeastern South China Sea and surrounding fluvial drainage basins: source and transport. Mar. Geol. 277, 48–60. doi:10.1016/j.margeo.2010.08.010.

Liu, Z.F., Zhao, Y.L., Colin, C., Stattegger, K., Wiesner, M.G., Huh, C.A., Zhang, Y.W., Li, X.J., Sompongchaiyakul, P., You, C.F., Huang, C.Y., Liu, J.T., Siringan, F.P., Le, K.P., Sathiamurthy, E., Hantoro, W.S., Liu, J.G., Tuo, S.T., Zhao, S.H., Zhou, S.W., He, Z.D., Wang, Y.C., Bunsomboonsakul, S., Li, Y.L., 2016. Source-to-sink transport processes of fluvial sediments in the South China Sea. Earth Sci. Rev. 153, 238–273. doi:10.1016/j.earscirev.2015.08.005.

Luo, K.W., Su, M., Liu, S., Shi, J.C., Wang, C., Chen, H., Yang, S.L., Lin, Z.X., Wei, L.J., 2023. Sea-level, climate, and oceanographic controls on recent deepwater hyperpycnites: a case example from the shenhu slope (northern South China Sea). Quat. Sci. Rev. 311, 108148. doi:10.1016/j.quascirev.2023.108148.

Lüthi, D., Le Floch, M., Bereiter, B., Blunier, T., Barnola, J.M., Siegenthaler, U., Raynaud, D., Jouzel, J., Fischer, H., Kawamura, K., Stocker, T.F., 2008. High-resolution carbon dioxide concentration record 650,000-800,000 years before present. Nature 453, 379–382. doi:10.1038/nature06949.

Mayer, L.M., 1994. Relationships between mineral surfaces and organic carbon concentrations in soils and sediments. Chem. Geol. 114, 347–363. doi:10.1016/0009-2541(94)90063-9.

McGee, D., Donohoe, A., Marshall, J., Ferreira, D., 2014. Changes in ITCZ location and cross-equatorial heat transport at the Last Glacial maximum, Heinrich Stadial 1, and the mid-Holocene. Earth Planet Sci. Lett. 390, 69–79. doi:10.1016/j.epsl.2013.12.043.

Meyers, P.A., 1997. Organic geochemical proxies of paleoceanographic, paleolimnologic, and paleoclimatic processes. Org. Geochem. 27, 213–250. doi:10.1016/S0146-6380(97)00049-1.

Mollenhauer, G., Kienast, M., Lamy, F., Meggers, H., Schneider, R.R., Hayes, J.M., Eglinton, T.I., 2005. An evaluation of 14C age relationships between co-occurring Foraminifera, alkenones, and total organic carbon in continental margin sediments. Paleoceanography and Paleoceanography 20, PA1016. doi:10.1029/2004PA001103.

Müller, P.J., Suess, E., 1979. Productivity, sedimentation rate, and sedimentary organic matter in the oceans —I. Organic carbon preservation. Deep-Sea Res., Part A 26, 1347–1362. doi:10.1016/0198-0149(79)90003-7.

North Greenland Ice Core Project members, 2004. High-resolution record of Northern hemisphere climate extending into the last interglacial period. Nature 431, 147–151. doi:10.1038/nature02805.

Perdue, E.M., Koprivnjak, J.F., 2007. Using the C/N ratio to estimate terrigenous inputs of organic matter to aquatic environments. Estuar. Coast Shelf Sci. 73, 65–72. doi:10.1016/j.ecss.2006.12.021.

Qu, T.D., Girton, J.B., Whitehead, J.A., 2006. Deepwater overflow through Luzon Strait. J. Geophys. Res., Oceans 111, C01002. doi:10.1029/2005JC003139.

Shen, X.Y., Hu, B.Q., Yan, H., Dodson, J., Zhao, J.T., Li, J., Ding, X., Li, Q., Wang, X.X., Xu, F.J., 2022. Reconstruction of Kuroshio intrusion into the south China sea over the last 40 kyr. Quat. Sci. Rev. 290, 107622. doi:10.1016/j.quascirev.2022.107622.

Shi, X.F., Wu, B., Qiao, S.Q., Yao, Z.Q., Hu, L.M., Bai, Y.Z., Hu, S., Sheng, J., Liu, Y.G., Liu, S.F., Wang, K.S., Zou, J.J., 2024. Distribution, burial fluxes and carbon sink effect of sedimentary organic carbon in the eastern China seas. Sci. China Earth Sci. 67, 3062–3082. doi:10.1007/s11430-024-1412-0.

Spratt, R.M., Lisiecki, L.E., 2016. A late Pleistocene sea level stack. Clim. Past 12, 1079–1092. doi:10.5194/cp-12-1079-2016.

Steinke, S., Mohtadi, M., Groeneveld, J., Lin, L.C., Löwemark, L., Chen, M.T., Rendle-Bühring, R., 2010. Reconstructing the southern South China Sea upper water column structure since the last Glacial Maximum: implications for the East Asian winter monsoon development. Paleoceanogr. Paleoclimatol. 25, A2219. doi:10.1029/2009PA00185.

Stuiver, M., Reimer, P.J., 2016. Extended 14C data base and revised CALIB 3.0 14C Age Calibration program. Radiocarbon 35, 215–230. doi:10.1017/S0033822200013904.

Sun, Y.B., Clemens, S.C., Morrill, C., Lin, X.P., Wang, X.L., An, Z.S., 2012. Influence of Atlantic meridional overturning circulation on the East Asian winter monsoon. Nat. Geosci. 5, 46–49. doi:10.1038/ngeo1326.

Tao, S.Q., Wang, A.J., Liu, J.T., Ye, X., Blattmann, T.M., Ran, C., Liu, Z.T., Wang, L., Yin, X.J., Zhang, H.L., Li, L., Ning, X.Y., Hung, C.C., Haghipour, N., 2023. The characteristics of sedimentary organic carbon burial in the shallow conduit portion of source-to-sink sedimentary systems in marginal seas. Geochem. Cosmochim. Acta 353, 92–111. doi:10.1016/j.gca.2023.05.006.

Tareq, S.M., Tanaka, N., Ohta, K., 2004. Biomarker signature in tropical wetland: lignin phenol vegetation index (LPVI) and its implications for reconstructing the paleoenvironment. Sci. Total Environ. 324, 91–103. doi:10.1016/j.scitotenv.2003.10.020.

Tong, G., Chen, L.L., Zhang, G.X., Liu, J., Chen, B., Xu, G., Liu, M., An, Y.H., Chen, D.X., 2023. High-resolution record of temporal change in organic matter burial over the past ~8,600 years on the northwestern continental slope of the South China Sea. Front. Earth Sci. 11, 1238920. doi:10.3389/feart.2023.1238920.

Wan, S., Jian, Z.M., 2014. Deep water exchanges between the South China Sea and the Pacific since the last glacial period. Paleoceanogr. Paleoclimatol. 29, 1162–1178. doi:10.1002/2013PA002578.

Wang, B., Lei, H.Y., Huang, F.F., Kong, Y., Pan, F.L., Cheng, W.D., Chen, Y., Guo, L.M., 2020. Effect of sea-level change on deep-Sea sedimentary records in the Northeastern South China Sea over the past 42 kyr. Geofluids 1–17. doi:10.1155/2020/8814545.

Wang, M.M., Wang, S.H., 2025. Origin and burial of sedimentary organic carbon in the northern South China Sea since the last glacial period. Palaeogeogr. Palaeoclimatol. Palaeoecol. 683, 113438. doi:10.1016/j.palaeo.2025.113438.

Wang, P.X., Li, Q.Y., Tian, J., 2014. Pleistocene paleoceanography of the South China Sea: progress over the past 20 years. Mar. Geol. 352, 381–396. doi:10.1016/j.margeo.2014.03.003.

Wang, X.X., Zhuo, H.T., Wang, Y.M., Mao, P.X., He, M., Chen, W.T., Zhou, J.W., Gao, S.M., Wang, M.H., 2018. Controls of contour currents on intra-canyon mixed sedimentary processes: insights from the Pearl River Canyon, northern South China Sea. Mar. Geol. 406, 193–213. doi:10.1016/j.margeo.2018.09.016.

Wang, Y.J., Cheng, H., Edwards, R.L., An, Z.S., Wu, J.Y., Shen, C.C., Dorale, J.A., 2001. A high-resolution absolute-dated Late Pleistocene monsoon record from Hulu Cave, China. Science 294, 2345–2348. doi:10.1126/science.1064618.

Waterson, E.J., Canuel, E.A., 2008. Sources of sedimentary organic matter in the Mississippi River and adjacent Gulf of Mexico as revealed by lipid biomarker and $\delta^{13}C_{TOC}$ analyses. Org. Geochem. 39, 422–439. doi:10.1016/j.orggeochem.2008.01.011.

Wei, B.B., Mollenhauer, G., Hefter, J., Grotheer, H., Jia, G.D., 2020. Dispersal and aging of terrigenous organic matter in the Pearl River Estuary and the northern South China Sea Shelf. Geochem. Cosmochim. Acta 282, 324–339. doi:10.1016/j.gca.2020.04.032.

Xiang, R., Chen, M.H., Li, Q.Y., Liu, J.G., Zhang, L.L., Lu, J., 2009. Planktonic foraminiferal records of East Asia monsoon changes in the southern South China Sea during the last 40,000 years. Mar. Micropaleontol. 73, 1–13. doi:10.1016/j.marmicro.2009.06.004.

Yin, S.R., Hernández-Molina, F.J., Fan, W.J., Li, J.B., 2024. Efficient organic carbon burial by bottom currents in the ocean: a potential role in climate modulation. Geophys. Res. Lett. 51, e2024GL109444. doi:10.1029/2024GL109444.

Yu, F.L., Zong, Y.Q., Lloyd, J.M., Huang, G.Q., Leng, M.J., Kendrick, C., Lamb, A.L., Yim, W.W.S., 2010. Bulk organic $\delta^{13}C$ and C/N as indicators for sediment sources in the Pearl River delta and estuary, southern China. Estuar. Coast Shelf Sci. 87, 618–630. doi:10.1016/j.ecss.2010.02.018.

Yu, H., Wu, Y., Zhang, J., Deng, B., Zhu, Z.Y., 2011. Impact of extreme drought and the three gorges Dam on transport of particulate terrestrial organic carbon in the Changjiang (Yangtze) river. J. Geophys. Res.: Earth Surf. 116. doi:10.1029/2011JF002012.

Zhang, C., Yang, S.Y., Huang, X.T., Dou, Y.G., Li, F.L., Xu, X.N., Hao, Q., Gao, J.H., 2022. Sea level change and Kuroshio intrusion dominated Taiwan sediment source-to-sink processes in the northeastern South China Sea over the past 244 kyrs. Quat. Sci. Rev. 287, 107558. doi:10.1016/j.quascirev.2022.107558.

Zhang, M.Y., Liu, X.T., Xu, F.J., Li, A.C., Gu, Y., Chang, X., Zhuang, G.C., Zhang, K.D., Bi, N.S., Wang, H.J., 2023. Organic carbon deposition on the inner shelf of the East China Sea constrained by sea level and climatic changes since the last deglaciation. J. Ocean Univ. China 22, 1300–1312. doi:10.1007/s11802-023-5476-x.

Zhang, Y.L., Kaiser, K., Li, L., Zhang, D.N., Ran, Y., Benner, R., 2014. Sources, distributions, and early diagenesis of sedimentary organic matter in the Pearl River region of the South China Sea. Mar. Chem. 158, 39–48. doi:10.1016/j.marchem.2013.11.003.

Zhao, H.C., Liu, Z.F., Lin, B.Z., Zhao, Y.L., 2024. Last glacial burial of woody debris in deep-sea sediments and its carbon cycling significance. Global Planet. Change 240, 104542. doi:10.1016/j.gloplacha.2024.104542.

Zhao, K., Wang, Y.J., Edwards, L., Cheng, H., Liu, D.B., Kong, X.G., Ning, Y.F., 2016. Contribution of ENSO variability to the East Asian summer monsoon in the late Holocene. Palaeogeogr. Palaeoclimatol. Palaeoecol. 449, 510–519. doi:10.1016/j.palaeo.2016.02.044.

Zheng, L.W., Ding, X.D., Liu, J.T., Li, D.W., Lee, T.Y., Zheng, X.F., Zheng, Z.Z., Xu, M.N.N., Dai, M.H., Kao, S.J., 2017. Isotopic evidence for the influence of typhoons and submarine canyons on the sourcing and transport behavior of biospheric organic carbon to the deep sea. Earth Planet Sci. Lett. 465, 103–111. doi:10.1016/j.epsl.2017.02.037.

Zheng, L.W., Hilton, R.G., Chang, Y.P., Yang, R.J., Ding, X.D., Zheng, X.F., Lee, T.Y., Lu, H.J., Lu, J.T., Lin, Y.S., Liu, J.T., Kao, S.J., 2024. Climate-regulation of organic carbon export in erosive mountain settings: a case study from Taiwan since the last glacial maximum. Quat. Sci. Rev. 334, 108687. doi:10.1016/j.quascirev.2024.108687.

Zheng, X.F., Kao, S.J., Chen, Z., Menviel, L., Chen, H., Du, Y., Wan, S.M., Yan, H., Liu, Z.H., Zheng, L.W., Wang, S.H., Li, D.W., Zhang, X., 2016. Deepwater circulation variation in the South China Sea since the last Glacial maximum. Geophys. Res. Lett. 43, 8590–8599. doi:10.1002/2016GL070342.

Zheng, Y., Ma, W., Wang, Y., Liu, Z., Xiu, P., 2023. Modeling dissolved organic carbon exchange across major straits and shelf breaks in the South China Sea. Prog. Oceanogr. 210, 102928. doi:10.1016/j.pocean.2022.102928.

Zhu, C., Wagner, T., Pan, J.M., Pancost, R.D., 2011. Multiple sources and extensive degradation of terrestrial sedimentary organic matter across an energetic, wide continental shelf. G-cubed 12, Q08011. doi:10.1029/2011GC003506.

Highlights

- Deep-water OC burial reflects coupled source inputs and transport–recycling processes.
- Radiocarbon age of OC is decoupled from source composition in deep-water settings.
- OC/SSA captures hydrodynamic sorting and mineral protection during OC transport.
- Sea-level and monsoon forcing imprint on OC burial via transport processes.

Appendix A Supplementary data

The following is the Supplementary data to this article:

Multimedia Component 1

Multimedia component 1

alt-text: Multimedia component 1

Queries and Answers

Q1

Query: Please check the article title and its casing amend if necessary.

Answer: Please amend the title casing to: Organic carbon burial drivers in the northeastern South China Sea since the last glacial.

Q2

Query: Please confirm that the provided **emails** “gcd@nju.edu.cn, clwang@nju.edu.cn” are the correct address for official communication, else provide an alternate e-mail address to replace the existing one, because private e-mail addresses should not be used in articles as the address for communication.

Answer: Reviewed

Q3

Query: Please check the hierarchy of the headings and sub-headings.

Answer: Checked. The heading hierarchy is correct. Thank you.

Q4

Query: The **citation(s)** ‘Tareq, 2004’ has been changed to match the author name/date in the reference list. Please check here and in subsequent occurrences, and correct if necessary.

Answer: Checked. The citation is correct as edited. Thank you.

Q5

Query: Have we correctly interpreted the following funding source(s) and country names you cited in your article: State Key Laboratory of Marine Geology, China; Tongji University, China; Natural Science Foundation of China, China?

Answer: Checked. Please correct "Natural Science Foundation of China" to "National Natural Science Foundation of China". All other funding sources and country names are correct as listed. Thank you.

Q6

Query: The **Uncited References** section comprises references that occur in the reference list but are not available in the body of the article text. Please cite each reference in the text or, alternatively, delete it. Any reference not dealt with will be retained in this section.

Answer: Done

Q7

Query: Please confirm that **given names and surnames** have been identified correctly and are presented in the desired order and please carefully verify the spelling of all authors' names.

Answer: Reviewed

Q8

Query: Your article is registered as a regular item and is being processed for inclusion in a regular issue of the journal. If this is NOT correct and your article belongs to a Special Issue/Collection please contact r.paree@elsevier.com immediately prior to returning your corrections.

Answer: Yes